Advances in Optics and Photonics

Dynamically tunable and active hyperbolic metamaterials

JOSEPH S. T. SMALLEY,[1,2,*] FELIPE VALLINI,[1] XIANG ZHANG,[2] AND YESHAIAHU FAINMAN[1]

[1]Department of Electrical and Computer Engineering, University of California, San Diego, La Jolla, California 92093, USA
[2]Department of Mechanical Engineering, University of California, Berkeley, Berkeley, California 94720, USA
*Corresponding author: jstsmalley@berkeley.edu

Received November 16, 2017; revised February 21, 2018; accepted February 23, 2018; published April 19, 2018 (Doc. ID 295367)

The first generation of hyperbolic metamaterials, metasurfaces, and naturally hyperbolic materials (HMMs) utilized the static and passive properties of their constituent metallic and dielectric components to achieve intriguing macroscopic behavior, such as imaging and focusing of light below the diffraction limit and the broadband modification to the rate of spontaneous emission. While promising, and operating from RF frequencies to the ultraviolet, many potential applications of early HMMs were spoiled by inflexible operation and dissipation losses. Recently, the use of dynamically tunable and active constituent materials has increased, guiding HMMs into more functional regimes. In this review we survey the state-of-the-art of tunable and active electromagnetic HMMs. Based on a firm theoretical foundation, we review the most recent experimental work on hyperbolic dispersion endowed with a tunable or active character. Additionally, we review proposed ideas that may inspire new experimental work and offer a comparison to other photonic platforms.

OCIS codes: (160.1190) Anisotropic optical materials; (160.3918) Metamaterials; (160.4330) Nonlinear optical materials; (300.1030) Absorption; (300.2140) Emission; (310.6628) Subwavelength structures, nanostructures
https://doi.org/10.1364/AOP.10.000354

1. Introduction. 356
2. Theoretical Background 358
2.1. Maxwell's Equations and the Constitutive Relations 360
2.2. Tunable Constituent Materials 361
2.2a. Optical Excitation 361
2.2b. Electrical Gating 362
2.2c. Phase-Change Materials 363
2.3. Active Constituent Materials 363
2.3a. Organic Dyes 363
2.3b. Rare-Earth Ions 365
2.3c. Bulk and Quantum Well Semiconductors 365
2.4. Surface and Bulk Plasmon and Phonon Polaritons 368

2.4a. Plasmon Polaritons . . . 368
2.4b. Phonon Polaritons . . . 369
2.5. Green's Function for Dipole Interactions . . . 370
2.5a. Isolated Dipole Near HMM . . . 370
2.5b. Purcell Factor . . . 371
2.5c. Two Dipoles Near HMM . . . 372
2.6. Propagating and Evanescent Waves in Complex Periodic Media . . . 372
2.6a. Finitely Periodic Systems: The Transfer Matrix Method . . . 372
2.6b. Finitely Periodic Systems: The Scattering Matrix Method . . . 374
2.6c. Infinitely Periodic Systems: Bloch Theory . . . 375
2.7. Effective Medium Theory . . . 379
2.7a. Dispersion Relation . . . 379
2.7b. Multilayer Metal–Dielectric System . . . 380
2.7c. Nanowire Array System . . . 380
2.7d. Higher-Order Approximations . . . 380
2.8. Resonance Cones . . . 381
3. Experimental Effects . . . 382
3.1. Broadband Purcell Effect . . . 382
3.1a. Emitters Near and Inside HMM . . . 382
3.1b. Thermal Emission of HMMs . . . 383
3.1c. Outcoupling Emission . . . 384
3.2. Hyperimaging and Focusing . . . 386
3.3. Plasmonic Spin Hall Effect . . . 386
3.4. Cherenkov Radiation . . . 387
3.5. Wave Mixing . . . 388
4. Applications . . . 388
4.1. High-Speed, High-Efficiency Light Sources . . . 388
4.2. Imaging and Focusing of Light with Super Resolution . . . 389
4.2a. Active Hyperlens . . . 389
4.2b. Hyperstructured Illumination Microscopy . . . 390
4.3. Electro-Optical and All-Optical Modulators . . . 391
4.4. Perfect Absorbers and Thermophotovoltaics . . . 391
5. Outlook . . . 392
5.1. 2D Materials . . . 392
5.2. Non-Reciprocal HMM . . . 394
5.2a. PT-Symmetric HMMs . . . 394
5.2b. Magneto-Optic HMM . . . 394
5.3. Long-Range Dipole Interactions . . . 395
5.4. Electronic Addressability . . . 396
5.5. Comparison to Other Systems . . . 397
5.5a. All-Dielectric Metamaterials . . . 397
5.5b. Single-Layer Plasmonics . . . 397
6. Conclusion . . . 398
Funding . . . 398
Acknowledgment . . . 398
References . . . 398

Dynamically tunable and active hyperbolic metamaterials

Joseph S. T. Smalley, Felipe Vallini, Xiang Zhang, and Yeshaiahu Fainman

1. INTRODUCTION

Hyperbolic metamaterials (HMMs) are naturally existing and engineered composite materials that exhibit hyperbolic dispersion for electromagnetic waves [1–5]. In the lossless, effective medium limit, the optical density of states (DOS) of HMMs has no upper bound [Fig. 1(a)], resulting in wave physics with extremely subwavelength scales [6,7], ultrafast speeds [8,9], and strong non-linear interactions [10,11]. Practically, the finite size of the constituent metal and dielectric components of HMMs sets an upper bound on the optical DOS [Fig. 1(b)], and absorptive losses mitigate the utility of states near the upper bound [Figs. 2(a) and 2(b)]. Additionally, HMMs generally have fixed behavior, dictated by the properties of the constituent materials and their relative concentration. Therefore, the static and dissipative character of conventional HMMs may be considered the primary roadblock to the widespread adoption of hyperbolic dispersion in practical technology, as well as to the observation of new scientific phenomena in the laboratory.

To address these challenges, research on HMMs with dynamically tunable and active properties has emerged at a rapid rate. Tunable HMMs consist of HMMs in which at least one of the constituent elements possesses tunable behavior, e.g., externally controlled dispersion [Fig. 1(c)]. Active HMMs consist of HMMs in which at least one of the constituent elements possesses active, non-dissipative behavior, e.g., optical gain [Fig. 2(c)]. Generally, the tunable and active properties may be considered forms of phase and absorption modulation, respectively, with the goal of controlling the real and imaginary parts of the refractive index of the constituent materials.

In this review, we report on the progress in tunable and active electromagnetic HMMs. In order to achieve sufficient depth, we place several restrictions on our review. First, as the title implies, we focus on HMMs with tunable and active functionality. Preference is given for dynamically tunable behavior though in some circumstances static tuning is reported if deemed sufficiently impactful. Second, aside from seminal works, we focus on reviewing work published in 2014 or later because earlier review papers have covered prior research [1–5]. Third, we give preference to fundamental theory and experimental demonstrations of new physics and device operation, relative to purely numerical device design. Lastly, we constrain ourselves to hyperbolic dispersion for electromagnetic waves, as the acoustic analog [12,13] is beyond our scope. These limitations aside, we have attempted to capture the status of the field without bias to frequency range of operation, choice of constituent materials, or geometric configuration. Therefore, we cover active HMMs from the terahertz to ultraviolet, using a myriad of natural and synthetic materials, in both the multilayer and nanowire array geometries. Nonetheless, for a field as rapidly expanding as active and tunable HMMs, it is extremely challenging, if not impossible, to achieve a complete survey of the field. We therefore apologize in advance to those researchers of active and tunable HMMs whose work we have inadvertently overlooked.

The review is organized as follows. In Section 2 we provide the necessary theoretical background for describing and understanding tunable and active hyperbolic

metamaterials. We begin from the most general formalism considering the tailorable electromagnetic response of constituent materials, proceed to propagation of waves in periodic structures made of these materials, and ultimately arrive at the effective medium approximation (EMA), from which hyperbolic dispersion derives its name. With a firm theoretical foundation, we review experimental realizations of dynamic HMMs in Section 3. As will be seen, HMMs affect all aspects of photons and electromagnetic waves, including the emission and absorption of radiation and wave propagation and modulation. In Section 4 we discuss emerging applications of dynamically tunable and active HMMs. These include high-speed and high-efficiency dynamic light sources, super-resolution imaging systems, and advanced thermophotovoltaic systems. Next, we provide an outlook on future hyperbolic devices and systems, discussing nascent proposals and experiments for tunable and active HMMs in Section 5. These include 2D HMMs, non-reciprocal HMMs, and long-range dipole interactions mediated by HMMs. Finally, in Section 6 we conclude the review. In organizing this review, we have thus striven to appeal to as broad an audience as possible, including theoreticians and experimentalists, newcomers, and experts. We hope that we have

Figure 1

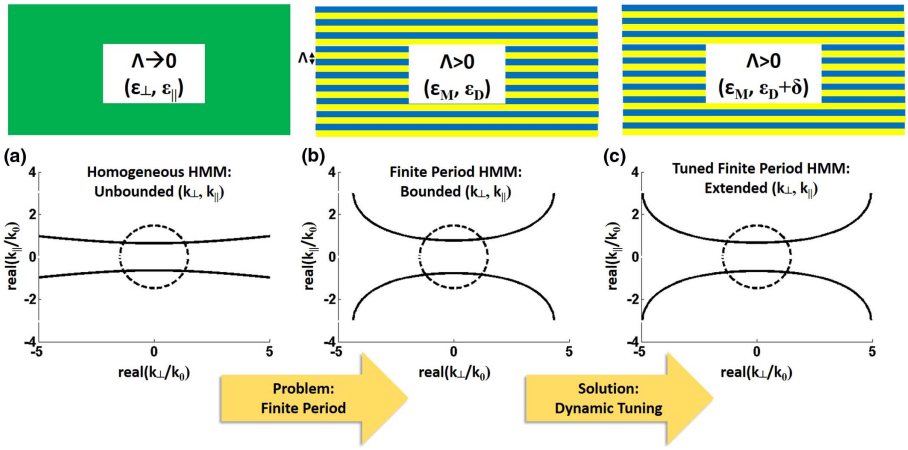

Solving the problem of static properties with dynamic tuning. (a) In the ideal effective medium limit, the unit cell length, or period, Λ, becomes vanishingly small with respect to the propagation wavelength, and the HMM is homogeneous with effective permittivity elements, $\epsilon_\perp$ and $\epsilon_\parallel$ of opposing sign, such that the relation between orthogonal wave-vector components, $k_\perp$ and $k_\parallel$, for a fixed temporal frequency defines a hyperbola. The optical density of states is defined mathematically by an integration over the hyperbola, which diverges, leading to intriguing wave physics such as far-field super-resolution imaging [6,7]. (For the calculation, we set Ag and Al_2O_3 as the constituent metal and dielectric at a vacuum wavelength of 365 nm and ignore losses.) (b) All practical HMMs have a finite period, which limits the maximum values of the wave-vector components. The finite period is a fundamental problem because the performance of the HMM devices, for example the resolution of the hyperlens, is determined by the maximum wave-vector values. (For the calculation we set both the Ag and Al_2O_3 layers, described by material permittivities, ϵ_M and ϵ_D, of opposing sign, as 30 nm thick.) (c) Dynamic tuning, for example, in the form of index modulation, increases the maximum value of the wave-vector components, and therefore extends the performance limit of the HMM. (For the calculation we decrease the refractive index of the Al_2O_3 layer by 4%.) In all calculations, the dashed curve describes the isotropic spherical dispersion of vacuum.

achieved our goal and eagerly await to witness the continued progress toward practical HMMs enabled by dynamically tunable and active properties.

2. THEORETICAL BACKGROUND

Hyperbolic dispersion emerges in a composite system when its constituent parts are described by elementary response functions of opposing sign. The electrical permittivity, $\tilde{\epsilon}$, and magnetic permeability, $\tilde{\mu}$, describe the response of a material to electric and magnetic fields, respectively. In general, both $\tilde{\epsilon}$ and $\tilde{\mu}$ are tensorial quantities, relating the vectorial nature of the driving fields and the material response. When the diagonal elements of the $\tilde{\epsilon}$ or $\tilde{\mu}$ tensor have opposing sign, the dispersion relation for waves polarized with their electric or magnetic field in a plane of anisotropy, respectively, describes a hyperbola [14]. Hence, engineered materials with this dispersion relation are known as hyperbolic metamaterials, and their quasi-two-dimensional counterparts, hyperbolic metasurfaces. Naturally existing materials may also exhibit hyperbolic dispersion [15]. Our use of the term HMMs will refer to all materials with hyperbolic dispersion, including metamaterials, metasurfaces, and natural materials.

Hyperbolic dispersion is achieved practically by combining constituent materials with opposing response functions. For example, when combined in the correct ratio, layered, isotropic metallic and dielectric materials described by $\epsilon' < 0$ and $\epsilon' > 0$, respectively (single prime denotes the real part and lack of tilde denotes isotropic) generate a hyperbolic dispersion relation for waves with wavelengths much larger than the layer thickness. Because all causal and passive materials exhibit dispersion and absorption, i.e., $\epsilon = \epsilon'(\omega) + i\epsilon''(\omega)$ (ω is angular frequency, double prime denotes imaginary part,

Figure 2

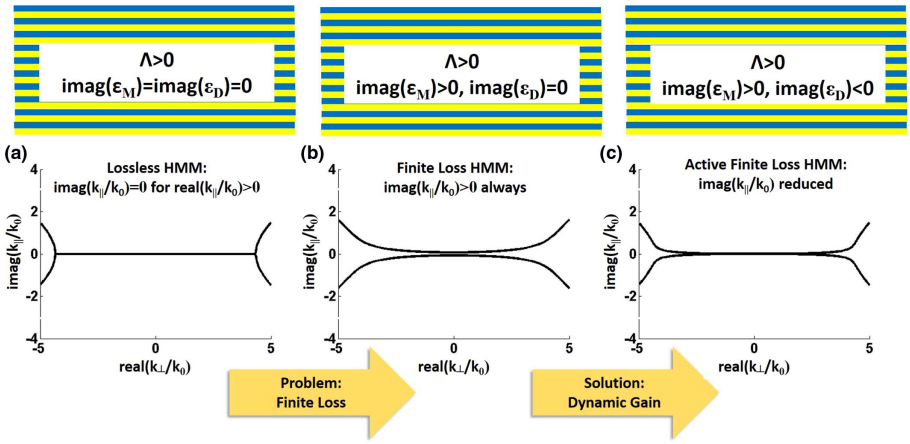

Solving the problem of loss with dynamic gain. (a) In the lossless but finite period case, the imaginary part of the wave-vector component is zero except for transverse wave-vector component values beyond the cutoff [see Fig. 1(b)]. (b) Finite imaginary values of the wave-vector components occur when finite loss is included in the HMM. The propagation loss increases with the magnitude of the transverse wave-vector component and thereby reduces performance of HMM devices. (For the calculation we set realistic losses uniformly in the Ag layers.) (c) Dynamic gain, for example, in the form of absorption modulation, decreases the maximum imaginary value of the wave-vector components, reduces propagation loss, and therefore extends the performance limit of the HMM. (For the calculation we add 2×10^4 cm^{-1} of material gain uniformly to the Al_2O_3 layers.)

and positive imaginary part denotes absorption), the spectral bandwidth of the resulting hyperbolic dispersion has a finite extent, within which the dissipation is non-zero.

In the absence of external degrees of freedom, the spectral width and location of hyperbolic dispersion may be modified by one of two ways: substitute one constituent material with a different material, or, change the ratio of the constituent metallic and dielectric materials. While useful, the static nature of these modifications is limited to situations in which dynamical variables, such as power flow or peak emission wavelength as a function of time, are not important. In most technologically relevant situations, however, the dynamics of physical quantities is crucial to the overall system performance.

Tunable and active hyperbolic dispersion is therefore much desired. Hyperbolic dispersion of a system becomes dynamically tunable inasmuch as the system's constituent parts have tunable or active properties. While the properties of all electromagnetic materials are, in principal, dependent on external perturbations, the design and synthesis of HMMs with active and tunable macroscopic properties is far from trivial. The most commonly used metallic components, for example, the noble metals, have an optical response fixed by their carrier concentration, and only weakly dependent on processing conditions. III-V semiconductors, which offer large optical gain coefficients in the visible and near-infrared, must be grown epitaxially, and are therefore difficult to combine with metallic components in a multilayer configuration. Operating in the mid-infrared with an all-semiconductor HMM appears to circumvent this problem [16], but the out-of-plane dipole moment associated with intersubband transitions is difficult to leverage for compensating losses [17]. Hence it is not obvious what the ideal system for tunable and active HMMs looks like. Nonetheless, it is the purpose of this review to cast a light onto the landscape from which a clearer picture may emerge.

In the following, we attempt to provide a suitable background for describing tunable and active hyperbolic dispersion. In this section we provide the theoretical foundation for understanding active and tunable HMMs, beginning with Maxwell's equations. Throughout, we stress the effects of the dispersive and absorptive parts of the constituent materials on the underlying equations. Figure 3 summarizes the constituent

Figure 3

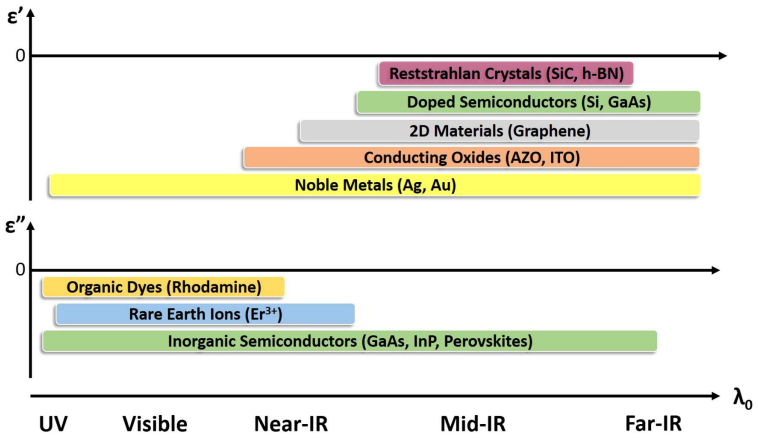

Materials for metallic and active behavior. The top and bottom panels show the spectral range over which various classes of materials behave as metals and gain media, with negative real and imaginary permittivity, respectively. (h-BN, hexagonal boron nitride; AZO, aluminum-doped zinc oxide; ITO, indium tin oxide).

materials that may behave as metals and gain media across the electromagnetic spectrum. In this review we discuss these materials with particular emphasis on combinations that yield hyperbolic dispersion with tunable or active behavior.

2.1. Maxwell's Equations and the Constitutive Relations

So far, we have introduced the electrical permittivity and magnetic permeability in a qualitative way. We now proceed to define these quantities more rigorously in the context of the electric field, **E**, electrical displacement, **D**, magnetic field, **H**, and magnetic flux density, **B**, which are related by Maxwell's equations and provide a classical description of the dynamics of charges and currents. Special attention will then be paid to externally controlling ϵ and μ, which in turn leads to the ability to externally control hyperbolic dispersion.

The macroscopic Maxwell's equations are [18]

$$\nabla \cdot \mathbf{D} = \rho_{\text{ext}}, \tag{1}$$

$$\nabla \cdot \mathbf{B} = 0, \tag{2}$$

$$\nabla \times \mathbf{E} = -\frac{\partial \mathbf{B}}{\partial t}, \tag{3}$$

$$\nabla \times \mathbf{H} = \frac{\partial \mathbf{D}}{\partial t} + \mathbf{J}_{\text{ext}}, \tag{4}$$

where ρ_{ext} and $\mathbf{J}_{\text{ext}}$ are external charge density and current density, respectively. The electric field and electric flux density are related through the macroscopic polarization, **P**, by

$$\mathbf{D} = \epsilon_0 \mathbf{E} + \mathbf{P} = \epsilon_0 \epsilon \mathbf{E}, \tag{5}$$

where $\epsilon_0 = 8.854 \times 10^{-12}$ F m^{-1} is the electrical permittivity of vacuum and

$$\epsilon = \epsilon'(\mathbf{k}, \omega) + i\epsilon''(\mathbf{k}, \omega) \tag{6}$$

is the generally, spatially dispersive, temporally dispersive, and absorptive relative permittivity. In writing the second of Eq. (5) we can then relate the material response linearly to the electric field by

$$\mathbf{P}(\mathbf{k}, \omega) = \epsilon_0 \chi(\mathbf{k}, \omega)\mathbf{E}(\mathbf{k}, \omega), \tag{7}$$

where $\chi(\mathbf{k}, \omega) = \epsilon(\mathbf{k}, \omega) - 1$. The assumption of a linear relation between **P** and **E** will be revisited momentarily, when we discuss dynamically controlled materials exhibiting tunable and active behavior. For now, we relate the magnetic field and the magnetic flux density through the macroscopic magnetization, **M**, by

$$\mathbf{B} = \mu_0 \mathbf{H} + \mathbf{M} = \mu_0 \mu \mathbf{E}, \tag{8}$$

where $\mu_0 = 4\pi \times 10^{-7}$ H m^{-1} is the magnetic permeability of vacuum, and

$$\mu = \mu'(\mathbf{k}, \omega) + i\mu''(\mathbf{k}, \omega) \tag{9}$$

is the generally, spatially dispersive, temporally dispersive, and absorptive relative permeability. The speed of wave propagation in vacuum, c, is related to the permittivity and permeability through $c = (\varepsilon_0 \mu_0)^{-1/2}$, and the vacuum wavenumber, k_0, and wavelength, λ_0, are related by $k_0 = 2\pi/\lambda_0 = \omega/c$.

2.2. Tunable Constituent Materials

Having presented the elementary framework for describing the linear response of materials to driving electromagnetic fields, we are now well positioned to more deeply describe the dependence of the materials properties on external fields. Necessarily, we are entering the regime of non-linear optics, wherein the interaction between multiple electric and/or magnetic fields leads to a system the dynamics of which are significantly more complex than in the linear case. Nonetheless, we hope to convey the relatively simple physical picture by which the combination of tunable constituent materials enables tunable hyperbolic dispersion.

Over a broad frequency range, the electromagnetic response of metals is well described by the Drude model. The Drude model directly accounts for the motion of free electrons and expresses the electrical permittivity as

$$\epsilon = \epsilon_b - \frac{\omega_p^2}{\omega^2 + i\omega\gamma} = \epsilon_b - \frac{\omega_p^2\tau^2}{1+\omega^2\tau^2} + i\frac{\omega_p^2\tau}{\omega(1+\omega^2\tau^2)}, \tag{10}$$

where the plasma frequency, ω_P, depends monotonically on the free carrier density, N, and effective electron mass, m_{eff}, through

$$\omega_P^2 = \frac{q^2 N}{\epsilon_0 m_{\text{eff}}}, \tag{11}$$

where $q = 1.602 \times 10^{-19}$ C is the electron charge, ϵ_b is the background permittivity describing bound charges, and γ is the damping rate and $\tau = \gamma^{-1}$ is the damping time.

In noble metals, such as gold and silver, N is fixed due to the elemental nature of the material, whereas γ can vary significantly depending on the technique used for material synthesis [19]. While the process-dependent damping of elemental metals holds modest value for designing variably absorbing metamaterials, the fixed carrier density is a major limitation.

The magnitude of N in non-elemental materials, such as transparent conducting oxides (TCOs), conversely, depends sensitively upon the processes by which the films are deposited and grown [20–22]. This enables a passive tunability to the electrical response, and thereby to the hyperbolic dispersion of HMMs with a TCO as the metallic element. Similarly, heavily doped semiconductors become metallic in the mid-infrared [16].

While useful, the passive tunability of N and γ has a similar effect as the passive tuning of the ratio of metallic to dielectric components in a composite system. Therefore, techniques to actively control the carrier density and damping rate are highly desirable. This can be found through optical excitation, electrical gating, and external temperature variation.

2.2a. Optical Excitation

The distinction between lattice and electron temperature is generally important for modeling dynamics of high-performance photonic devices, including, for example, vertical-cavity surface-emitting lasers [23,24]. Under the influence of a strong optical field, the random phase approximation may be used to describe the intraband lattice and electron dynamics of a metal. In this case the intraband part of the permittivity is expressed as [11]

$$\epsilon(\omega, T_L, T_e) = \epsilon_\infty - \frac{\omega_p^2}{\omega(\omega + i\gamma(\omega, T_L, T_e))}, \tag{12}$$

where T_L and T_e are the temperatures of the lattice and free electron gas, respectively. In the absence of external optical excitation, $T_L = T_e$. However, under the influence of a sufficiently strong external field, T_e can exceed T_L by an order of magnitude, for example from room temperature to 3000 K. This mechanism can be used to construct a high-contrast and extremely compact all-optical switch in an HMM platform, as will be discussed in Subsection 2.3.

Whereas external control of γ directly changes the imaginary part of the metal permittivity, the dependence of the real part on intense fields is described by the Kerr effect. Namely, in the presence of a sufficiently strong field, we define a non-linear permittivity, ϵ_{NL}, as

$$\epsilon_{\mathrm{NL}} = \epsilon + \chi^{(3)} I_p, \tag{13}$$

where $\chi^{(3)}$ is the third-order non-linear susceptibility and I_p is the intensity of the external optical pump [25]. We will see in Subsection 2.3 that the Kerr effect is also useful for HMM-based all-optical switching. Generally, the Kerr effect can apply to the constituent dielectric or metallic components in an HMM, or both simultaneously. However, often the effect in one of the components will dominate the ultimate effect on the hyperbolic dispersion, as will be shown in subsequent sections.

2.2b. Electrical Gating

The carrier density in two-dimensional (2D) materials exhibits a remarkably strong dependence on external static fields. In graphene, for example, the density of electrons is externally controllable with a gate voltage, V_G, that changes the Fermi level. The permittivity of graphene may be expressed in terms of its conductivity, σ, by [26]

$$\epsilon(\omega, V_b) = 1 - i\frac{\sigma(\omega, \mu_C)}{\omega \epsilon_0 t_g}, \tag{14}$$

where t_g is the thickness of monolayer graphene and μ_C is the externally controlled chemical potential. The latter depends on V_G through

$$|\mu_C| = \hbar \nu_F \sqrt{\pi |a_0 (V_G - V_{\mathrm{Dirac}})|}, \tag{15}$$

where $\hbar = 1.05 \times 10^{-34}$ J s is the reduced Planck's constant, $\nu_F \approx 10^6$ m s^{-1} is the Fermi velocity at the Dirac point, $a_0 = 9.6 \times 10^{16}$ (m V)$^{-1}$, and V_{Dirac} is the offset bias determined by doping and impurities. With the chemical potential known, the permittivity can then be calculated from the conductivity. The latter is

$$\begin{aligned}\sigma(\omega, \mu_C) = &-i\frac{4\pi q^2 k_B T}{h^2(\omega - i2\tau)}\left[\mu_C (k_B T)^{-1} + 2\ln\left(e^{-\mu_C (k_B T)^{-1}} + 1\right)\right] \\ &- \frac{i4\pi q^2 (\omega - i2\tau)}{h^2}\int_0^\infty \frac{f_D(-\zeta) - f_D(\zeta)}{(\omega - i2\tau)^2 - 16\pi\zeta h^{-1}}\mathrm{d}\zeta,\end{aligned} \tag{16}$$

where

$$f_D(\zeta) = \frac{1}{\exp((\zeta - \mu_C)(k_B T)^{-1}) + 1} \tag{17}$$

is the Fermi–Dirac function, $h = 6.63 \times 10^{-34}$ J s is Planck's constant, $k_B = 1.38 \times 10^{-23}$ J K^{-1} is Boltzmann's constant, and T is the temperature. For the case of multilayer graphene less than or equal to six layers, Eq. (16) may be simply scaled by the number of layers to find the multilayer conductivity [26].

2.2c. Phase-Change Materials

Thus far we have described mechanisms by which the carrier density, N, and electron damping rate, γ, may be modified dynamically in the constituent metallic and dielectric materials, including optical excitation and electrical gating. External temperature is another mechanism by which optical properties can be changed. In particular, control of the external temperature causes certain materials to undergo solid-state phase changes. For example, vanadium oxide (VO_2) changes from insulating to metallic at a modest $T = 68°C$, making it useful as a constituent material in a practically tunable HMM [27,28]. The permittivity of a phase-change material may be conveniently modeled as a sum of Lorentz oscillators and a Drude term of the form

$$\epsilon(\omega) = \epsilon_\infty + \sum_{n=0}^{\infty} \frac{A_n \omega_n}{\omega_n^2 - \omega^2 - i\gamma_n \omega} + \frac{-B\gamma}{\omega^2 + i\gamma\omega}, \tag{18}$$

where the second and third terms account for bound and free electrons, respectively. A_n describes the strength of the bound transition centered at ω_n with damping γ_n and B is related to the strength of the free electron response. Below and above the insulator-to-metal transition temperature $B = 0$ and $B > 0$, respectively. Because the external temperature can cause a complete change in optical character, phase-change materials can play a dramatic role in tuning a metamaterial from elliptic to hyperbolic dispersion.

2.3. Active Constituent Materials

In earlier sections we have mentioned the complex nature of the material response, where the imaginary part is responsible for absorption. In this section we provide further detail on this point with the goal of describing constituent materials that exhibit optical gain. Optical gain necessarily requires external control mechanisms because all causal materials are inherently passive.

2.3a. Organic Dyes

To date, most active HMMs have used organic dye molecules as the gain media because dyes are inexpensive and fairly easy to incorporate into conventional multilayer structures. Theoretically, the easiest way to model gain in an HMM is to use a constituent dielectric with an imaginary part that opposes the sign of the imaginary part of the constituent metal. Here, we use the convention that $\epsilon'' > 0$ corresponds to loss and $\epsilon'' < 0$ corresponds to gain. A more rigorous description of optical gain accounts for the electric field and material polarization self-consistently. This method was first used in the analysis of generic metamaterials with gain, and later for studying active HMMs for improved imaging performance [29–32]. A self-consistent, time-domain approach is often necessary because, in the presence of gain, the dispersion of the HMM may significantly change relative to the absence of gain due to the Kramers–Kronig relations. In turn, the interaction between a propagating electromagnetic field and the material gain changes as the HMM dispersion changes, until eventually a steady state is reached. One of the most interesting features of the self-consistent model is that the effective gain coefficient for the metamaterial can exceed the gain coefficient of the constituent gain material in isolation [29]. This occurs because the metamaterial supports strong electric fields that effectively amplify the intrinsic gain coefficient of the constituent gain material, overcoming the absorption coefficient associated with the constituent metal. Hence using a less rigorous approach such as the naive inclusion of a negative ϵ'' may lead to either overestimated or underestimated results depending on the situation.

Assume a four-level system with the charge carrier population density in each level given by $N_l (l = 0, 1, 2, 3)$. Carriers are pumped at the rate R_{03} from level 0 to level 3,

decay quickly non-radiatively between level 3 and level 2 and between level 2 and level 0 at the rates τ_{32} and τ_{10}, respectively. Between levels 2 and 1, the decay is slower and partially radiative at the rate τ_{21}. Transitions between levels 3 and 1, 3 and 0, or 2 and 0, are generally deemed forbidden. An optical pump with the energy $E_{30} = E_3 - E_0 = \hbar\omega_{30}$ excites carriers from the ground state (level 0) to level 3, and optical emission occurs with the energy $E_{21} = E_2 - E_1 = \hbar\omega_{21}$. The dynamics of this four-level system are described by

$$\frac{\partial N_3}{\partial t} = R_{03}N_0 - \frac{N_3}{\tau_{32}}, \tag{19}$$

$$\frac{\partial N_2}{\partial t} = \frac{N_3}{\tau_{32}} - \frac{N_2}{\tau_{21}} + \frac{1}{\hbar\omega_{21}}\mathbf{E}\cdot\frac{\partial \mathbf{P}}{\partial t}, \tag{20}$$

$$\frac{\partial N_1}{\partial t} = \frac{N_2}{\tau_{21}} - \frac{N_1}{\tau_{10}} - \frac{1}{\hbar\omega_{21}}\mathbf{E}\cdot\frac{\partial \mathbf{P}}{\partial t}, \tag{21}$$

$$\frac{\partial N_0}{\partial t} = -R_{03}N_0 + \frac{N_1}{\tau_{10}}, \tag{22}$$

where the term $\frac{1}{\hbar\omega_{21}}\mathbf{E}\cdot\frac{\partial \mathbf{P}}{\partial t}$ denotes stimulated emission and absorption when positive and negative, respectively. The polarization, $\mathbf{P}$, is described as a forced harmonic oscillator driven by the local electric field, $\mathbf{E}$, according to

$$\frac{\partial^2 \mathbf{P}(t)}{\partial t^2} + \gamma_{21}\frac{\partial \mathbf{P}(t)}{\partial t} + \omega_{21}^2\mathbf{P}(t) = -\sigma_{21}\Delta N(t)\mathbf{E}(t), \tag{23}$$

where $\Delta N = N_2 - N_1$ and σ_{21} is the coupling strength between $\mathbf{P}$ and $\mathbf{E}$, with a typical value of 10^{-4} $\mathrm{C^2\,kg^{-1}}$. Typical values of the time constants are $\tau_{32} = \tau 10 = 50$ fs and $\tau_{21} = 5$ ps, with a total electron density of $N = N_0 + N_1 + N_2 + N_3 = 5 \times 10^{17}$ $\mathrm{cm^{-3}}$ for dye molecules. Equations (19)–(23) may be solved through the finite-difference time-domain method [29], where the field, polarization, and population densities are sequentially updated at each point in space along each time step. A strong pump wave excites the total carrier population, initially in the ground state, and a second, weaker, wave probes the metamaterial as the system evolves.

For sufficiently weak pumping wherein the probe responds linearly to the pump ($|\mathbf{E}| < 10^4$ $\mathrm{V\,m^{-1}}$ in [29]), a simpler model for the optical gain can be used, circumventing the self-consistent calculation. In this case, the magnitude of the polarization takes the form

$$P = \epsilon_0(\chi' + \chi'')E, \tag{24}$$

where

$$\chi'(\omega) = -\frac{\chi_0''\Delta x(\omega)}{1 + \Delta x(\omega)^2}, \tag{25}$$

$$\chi''(\omega) = \frac{\chi_0''(\omega)}{1 + \Delta x(\omega)^2}, \tag{26}$$

$\Delta x(\omega) = \frac{2(\omega-\omega_{21})}{\gamma_{21}}$, and $\chi_0 = \frac{\sigma_{21}\Delta N}{\epsilon_0\omega_{21}\gamma_{21}}$. Further, in the linear case, the permittivity may be approximated as an explicit function of the pumping rate according to a simple Lorentzian function [32]:

$$\epsilon(\omega) = 1 + \frac{\omega_g^2}{\omega^2 - \omega_{21}^2 + i\omega\gamma_{21}}, \tag{27}$$

where

$$\omega_g = \sqrt{\frac{RN\sigma_{21}}{\gamma_{21}\epsilon_0}}. \tag{28}$$

Finally, if the refractive index of the dielectric host for the dye molecules, n_h, is much larger than the real and imaginary parts of χ, then in the linear pumping regime we can approximate the frequency-dependent effective index of the four-level system as [31]

$$n'(\omega) = \sqrt{n_h^2 - \frac{2 + n_h^2}{3\epsilon_0} \sum_{i=30,21} \frac{\omega_i^2 - \omega^2}{(\omega_i^2 - \omega^2) + 4\gamma_i^2\omega^2}\sigma_i\Delta_i}, \tag{29}$$

$$n''(\omega) = -\frac{2 + n_h^2}{6n_h\epsilon_0} \sum_{i=30,21} \frac{2\gamma_i\omega}{(\omega_i^2 - \omega^2) + 4\gamma_i^2\omega^2}\sigma_i\Delta_i. \tag{30}$$

2.3b. Rare-Earth Ions

Rare-earth ions are an attractive gain media to incorporate into HMMs because they may be co-sputtered with oxides providing a more stable gain media than organic dyes without significant added complexity.

For example, erbium oxide (Er_2O_3) can be co-sputtered with aluminum oxide (Al_2O_3) to form a light-emitting [33] oxide film. Enhancement in photoluminescence and up-conversion efficiency of Er^{3+} was achieved by placing Ag films of varying thickness atop the Er-doped oxide layer. In principle, one should be able to achieve a multilayer metal-oxide geometry in which the oxide layer contains co-sputtered Er ions. The precise gain profile of Er-doped oxides depends on the exact transition and host oxide. The amplification process in Er-doped media is most often modeled by a three-level system [34]. In this case the lasing transition occurs between the first excited state and the ground state. Therefore, unlike the four-level system used for modeling dyes, population inversion requires a more substantial pumping rate to reduce the ground-state population [34].

2.3c. Bulk and Quantum Well Semiconductors

Beyond isolated emitters, bulk and one-dimensional quantum heterostructures, i.e., quantum wells (QWs), are the most challenging gain media to incorporate into HMMs. To date, a self-consistent description of the dynamics of charge carriers and photons in a metal-QW composite medium exhibiting hyperbolic dispersion has yet to be demonstrated, though advanced models for self-consistent QW gain dynamics have been put forth [35]. Here we outline the origin of gain in QW semiconductors, which can be incorporated into linearly pump-dependent models for active HMMs [36,37].

In semiconducting dielectric components, N describes the number of free electron-hole pairs. In the two-band effective mass approximation, assuming an undoped semiconductor [38],

$$N = \int f_2(\hbar\omega)(1 - f_1(\hbar\omega))\rho_E \mathrm{d}\omega, \tag{31}$$

where f_2 and f_1 are the quasi-Fermi levels of the conduction and valence bands, respectively, and ρ_E is the electronic density of states. The attenuation, α, experienced by a propagating wave in the semiconductor decreases monotonically with increasing

N. The optical gain, g, is therefore an increasing function of N, and may be written as [39]

$$g(\hbar\omega; N) = \frac{n'\epsilon_0 c m_0 \omega}{\pi q^2} \int |M_T(E_{21})| \rho_E(E_{21}) f_{21}(\omega, N) L_B(\hbar\omega - E_{21}) \mathrm{d}E_{21}, \tag{32}$$

where M_T is the transition momentum matrix element, L_B is the homogeneous broadening line shape function, E_{21} is the transition energy between the conduction and valence band states, n' is the refractive index, and m_0 is the free electron mass. In bulk media, the integration in Eq. (32) is performed from the conduction band edge to infinity, whereas in QW media, it is performed from the first conduction subband edge to infinity. The magnitude of the electronic density of states in the QW is determined by the valence band and conduction band effective masses, m_V and m_C, respectively, while the peak spectral location of the nth subband is determined by the energy difference between the conduction and valence band, $E_{C,n} - E_{V,n}$. Finally, the broadening is given by the intraband scattering time, τ_{in}, leading to

$$\rho_E(\omega) = \frac{m_C m_V}{\pi \hbar^2 L_{QW}(m_C + m_V)} \left(\frac{1}{2} + \frac{1}{\pi} \tan^{-1} \left(\hbar\omega - \frac{(E_{C,n} - E_{V,n})\tau_{\text{in}}}{\hbar} \right) \right), \tag{33}$$

where L_{QW} is the thickness of an individual well. The inversion factor is a function of the quasi-Fermi levels in the conduction and valence bands, F_C and F_V, respectively, and is given by

$$\begin{aligned} f_{21}(\omega, N) &= f_2(\omega, N) - f_1(\omega, N) \\ &= \left[\exp\left(\frac{E_C - F_C}{k_B T} \right) + 1 \right]^{-1} - \left[\exp\left(\frac{E_V + F_V}{k_B T} \right) + 1 \right]^{-1}, \end{aligned} \tag{34}$$

where T is the average temperature, and E_C and E_V are the conduction and valence band energies, respectively. The latter are calculated by the parabolic band approximation,

$$E_C = E_{C,n} + \frac{m_V}{m_C + m_V} (\hbar\omega - E_{G,n}), \tag{35}$$

$$E_V = E_{V,n} - \frac{m_C}{m_C + m_V} (\hbar\omega - E_{G,n}), \tag{36}$$

where $E_{G,n}$ is bandgap energy between the nth set of subbands. In practice Eq. (32) is solved by first solving Eqs. (35) and (36) given input values for L_{QW}, the bandgap energy of the well and barrier materials, $E_{G,Q}$ and $E_{G,B}$, respectively, and the conduction and valence band offsets between the well and barrier, ΔE_C and ΔE_V, respectively [39]. Then Eq. (34) is solved by numerically finding values of F_C that satisfy

$$\begin{aligned} N = &\frac{4\pi m_0}{\hbar^2 L_{QW}} \sum_n \int_{E_{C,n}}^{E_{C,n} + \Delta E_C} \left[1 + \exp\left(\frac{E - F_C}{k_B T} \right) \right]^{-1} \mathrm{d}E \\ &+ \frac{4 m_0}{\pi^{1/2}} \left(\frac{2\pi m_0}{h^2} \right)^{3/2} \int_{E_{C,n} + \Delta E_C}^{\infty} E^{1/2} \left[1 + \exp\left(\frac{E - F_C}{k_B T} \right) \right]^{-1}, \end{aligned} \tag{37}$$

and values of F_V that satisfy

$$N = \frac{4\pi m_0}{\hbar^2 L_{QW}} \sum_n \int_{E_{V,n}}^{E_{V,n}+\Delta E_V} \left[1 + \exp\left(\frac{E - F_V}{k_B T}\right)\right]^{-1} \mathrm{d}E + \frac{4m_0}{\pi^{1/2}} \left(\frac{2\pi m_0}{h^2}\right)^{3/2} \int_{E_{V,n}+\Delta E_V}^{\infty} E^{1/2} \left[1 + \exp\left(\frac{E - F_V}{k_B T}\right)\right]^{-1}, \tag{38}$$

where the carrier density is treated as an input parameter. For all calculations we assume room temperature operation, such that $k_B T = 0.0259$ eV. We approximate M_T as a constant with respect to ω, but do account for its polarization dependence.

The optical gain spectra of a 10 nm InGaAsP QW is shown in Fig. 4 with the carrier density and temperature as parameters, calculated from Eq. (32). The magnitude of N in semiconductors, such as InGaAsP multiple quantum wells (MQW), depends sensitively upon external pumping conditions. By Kramers–Kronig relations, the phase delay experienced by a propagating wave also changes with N. This enables an active tunability to the electrical response and thereby to the hyperbolic dispersion of HMMs with InGaAsP MQW as the dielectric constituent.

For plane wave propagation in an inverted medium with $\epsilon'' < 0$, the optical gain relates to the semiconductor permittivity through [40]

$$g = -\alpha = k_0 \frac{\epsilon_D''}{\sqrt{\epsilon_D'}}, \tag{39}$$

under the assumption that $\epsilon_D' \gg \epsilon_D''$. A more exact determination of the complex permittivity from the attenuation or gain coefficient follows from its definition as the square of the complex refractive index. Namely,

$$\epsilon_D' = n'^2 - n''^2 = n'^2 - \left(\frac{\alpha\lambda_0}{4\pi}\right)^2, \tag{40}$$

$$\epsilon_D'' = 2n'n'' = n' \frac{\alpha\lambda_0}{2\pi}. \tag{41}$$

Figure 4

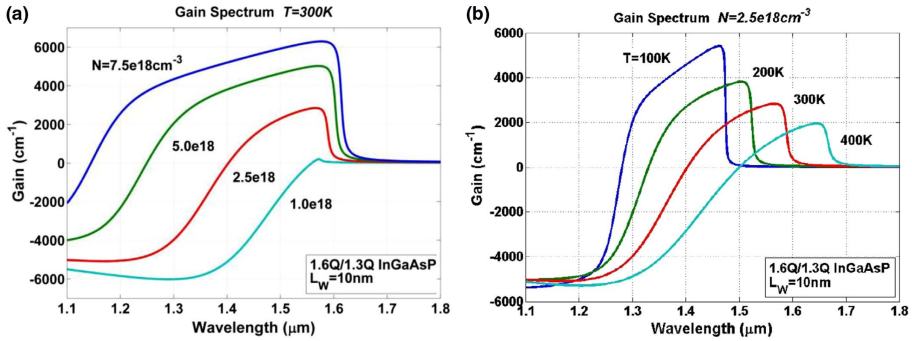

Optical gain spectra of a 10 nm InGaAsP QW [39]. (a) Gain spectra with temperature fixed at $T = 300$ K and carrier density, N, ranging from 1×10^{18} cm^{-3} to 7.5×10^{18} cm^{-3}. (b) Gain spectra with N fixed at 2.5×10^{18} cm^{-3} and T ranging from 100 K to 400 K. The well and barrier materials are InGaAs and InGaAsP, respectively. © 2014 IEEE. Reprinted, with permission, from Smalley *et al.*, IEEE J. Quantum Electron. **50**, 175–185 (2014) [39].

2.4. Surface and Bulk Plasmon and Phonon Polaritons

The interface between two media with opposing sign of the real part of the electrical permittivity supports a surface wave known as a polariton. When the medium with negative permittivity attains its character from the motion of free electrons, the polariton is a plasmon polariton. On the other hand, when lattice vibrations are responsible for the negative permittivity, the polariton is a phonon polariton. The dispersion relations for these polaritons, which form the foundation of all HMMs, are now presented.

2.4a. Plasmon Polaritons

The dispersion relation for a surface plasmon polariton (SPP) at the interface between a semi-infinite metal and a semi-infinite dielectric is

$$k_{\mathrm{SPP}}(\omega) = k_0\sqrt{\frac{\epsilon_M(\omega)\epsilon_D(\omega)}{\epsilon_M(\omega)+\epsilon_D(\omega)}}, \tag{42}$$

where k_{SPP} is the magnitude of the SPP wave vector. Expanding k_{SPP} into its real and imaginary parts, we have

$$k'_{\mathrm{SPP}}(\omega) = k_0\frac{\epsilon'_M(\epsilon'^2_D+\epsilon''^2_D)+\epsilon'_D(\epsilon'^2_M+\epsilon''^2_M)}{\epsilon'^2_M+\epsilon''^2_M+\epsilon'^2_D+\epsilon''^2_D+2(\epsilon'_M\epsilon'_D+\epsilon''_M\epsilon''_D)}, \tag{43}$$

$$k''_{\mathrm{SPP}}(\omega) = k_0\frac{\epsilon''_M(\epsilon'^2_D+\epsilon''^2_D)+\epsilon''_D(\epsilon'^2_M+\epsilon''^2_M)}{\epsilon'^2_M+\epsilon''^2_M+\epsilon'^2_D+\epsilon''^2_D+2(\epsilon'_M\epsilon'_D+\epsilon''_M\epsilon''_D)}. \tag{44}$$

The SPP propagation length is

$$L_{\mathrm{SPP}} = \frac{1}{2k''_{\mathrm{SPP}}}, \tag{45}$$

while the penetration depth into the metal and dielectric are

$$d_{\mathrm{SPP},M} = \left|\frac{1}{\sqrt{\epsilon_M k_0^2 - k_{\mathrm{SPP}}^2}}\right| \tag{46}$$

and

$$d_{\mathrm{SPP},D} = \left|\frac{1}{\sqrt{\epsilon_D k_0^2 - k_{\mathrm{SPP}}^2}}\right|, \tag{47}$$

respectively. In the negligible loss, long wave-vector limit, the temporal frequency of the SPP is

$$\omega_{SP} = \frac{\omega_P}{\sqrt{1+\epsilon_M}}. \tag{48}$$

As shown in Subsections 2.2 and 2.3, both the real and imaginary parts of both the constituent metal and dielectric materials may be externally controlled by a number of different mechanisms. Thus, the dispersion, loss, and penetration depth of SPPs may all be modified by perturbing the metal and dielectric.

Two SPPs may be brought in close proximity to each other by creating a metal–dielectric–metal or dielectric–metal–dielectric multilayer, where the middle layer has a thickness, t, small compared to the vacuum wavelength. When the semi-infinite bounding layers of this sandwich are identical, the dispersion relation takes the form

$$\tanh k_1 a = -\frac{k_2 \epsilon_1(\omega)}{k_1 \epsilon_2(\omega)}, \tag{49}$$

$$\tanh k_1 a = -\frac{k_1 \epsilon_2(\omega)}{k_2 \epsilon_1(\omega)}, \tag{50}$$

where a is the thickness of the middle layer, $k_1 = \sqrt{\epsilon_1 k_0^2 - k_{\mathrm{SPP}}^2}$, and $k_2 = \sqrt{\epsilon_2 k_0^2 - k_{\mathrm{SPP}}^2}$. Coupling between SPPs leads to a splitting in their characteristic frequency, which may be analytically approximated in the low-loss limit as [18]

$$\omega_+ = \frac{\omega_P}{\sqrt{1+\epsilon_M}} \sqrt{1 + \frac{2\epsilon_M \exp(-2k_{\mathrm{SPP}} t)}{1+\epsilon_M}}, \tag{51}$$

$$\omega_- = \frac{\omega_P}{\sqrt{1+\epsilon_M}} \sqrt{1 - \frac{2\epsilon_M \exp(-2k_{\mathrm{SPP}} t)}{1+\epsilon_M}}. \tag{52}$$

Conversely, for a fixed temporal frequency, the system will support two SPPs, $k_{\mathrm{SPP},+}$ and $k_{\mathrm{SPP},-}$, where $k_{\mathrm{SPP},-} < k_{\mathrm{SPP}} < k_{\mathrm{SPP},+}$. The two SPPs are known as long-range and short-range SPP due to fact that one of them has a significantly larger L_{SPP} than the other [41].

Adding more layers to the metal–dielectric system will lead to further splitting of the characteristic temporal and spatial frequencies [42]. Consider a repeating sequence of metal and dielectric layers with the period $\Lambda = t_M + t_D$, where t_M and t_D are the metal and dielectric layer thicknesses, respectively. For a fixed spatial frequency, k, the spectral bandwidth, $\Delta\omega$, of the coupled SPP system is inversely proportional to Λ. Similarly for a fixed temporal frequency, ω, the angular bandwidth, Δk, is inversely proportional to Λ. For a fixed Λ, the number of resonances within $\Delta\omega$ and Δk is proportional to the number of periods, N_p. Beyond a three-layer system, the SPPs take on the character of bulk modes and are therefore called bulk plasmon polaritons (BPPs) [43,44]. The BPPs are the information carriers in hyperbolic media. Hence creating active and tunable HMMs requires tuning and providing gain to BPPs. As with a single SPP, this is achieved by dynamically controlling the complex permittivity (or permeability) of the constituent metal and dielectric layers.

2.4b. Phonon Polaritons

In polar crystals, surface phonon polaritons (SPhPs) may be observed to propagate in the Restrahlan band, which is the range of frequencies between the resonances of the transverse optical phonon, ω_{TO}, and longitudinal optical phonon, ω_{LO} [45]. The permittivity of uniaxial polar crystals is anisotropic, with distinct components describing the optical response parallel and perpendicular to the optical axis. In many cases these components may be described by a single Lorentzian function of the form [46]

$$\epsilon_\perp(\omega) = \epsilon_{\infty,\perp}\left(1 + \frac{\omega_{\mathrm{LO},\perp}^2 - \omega_{\mathrm{TO},\perp}^2}{\omega_{\mathrm{TO},\perp}^2 - \omega^2 - i\omega\gamma_\perp}\right), \tag{53}$$

$$\epsilon_{\parallel}(\omega) = \epsilon_{\infty,\parallel}\left(1 + \frac{\omega_{\mathrm{LO},\parallel}^2 - \omega_{\mathrm{TO},\parallel}^2}{\omega_{\mathrm{TO},\parallel}^2 - \omega^2 - i\omega\gamma_{\parallel}}\right). \tag{54}$$

The magnitude of the wave vector propagating along the optical axis is then described by the dispersion relation [46]

$$k_{\mathrm{SPhP}} = k_0\sqrt{\epsilon_{\perp}\left(1 - \frac{k_{\perp}}{\epsilon_{\parallel}k_0}\right)}, \tag{55}$$

where $k_{\perp}$ is the wave-vector component normal to the optical axis, usually treated as an independent, real-valued quantity. Similar to SPPs, the properties of SPhPs can be tuned by perturbing the polar crystal externally, for example with phase-change thin films atop the polar crystal [47].

Whereas SPhPs arise in naturally existing anisotropic materials with atomic-scale periodicity, the description of engineered HMMs as uniaxial crystals arises from the effective medium approximation, which is detailed in Subsection 2.8.

2.5. Green's Function for Dipole Interactions

To describe the interaction between a dipole and HMM, as well as dipole–dipole interactions in the presence of HMMs, the Green's function method is often employed. By treating a quantum emitter as a point source, its radiation field may be described as an infinite sum of plane waves, each with a particular direction, or k-vector. Each plane wave will exhibit a characteristic reflection and transmission frequency spectrum. By integrating over the angular spectrum, the emission rate of the dipole near an HMM can be determined for a particular temporal frequency. The reflection and transmission properties of an HMM will be discussed in Subsection 2.6. Now we focus on the Green's function.

2.5a. Isolated Dipole Near HMM

The Green's function, $\mathbf{G}$, is the impulse response at a location r' to a point source located at r. It satisfies the Helmholtz equation [48]

$$\nabla \times \nabla \mathbf{G}(\mathbf{r}, \mathbf{r}'; \omega) - \epsilon(\omega)\frac{\omega^2}{c^2}\mathbf{G}(\mathbf{r}, \mathbf{r}'; \omega) = \mathbf{1}\delta(\mathbf{r} - \mathbf{r}'). \tag{56}$$

Using a plane wave basis, we may write the Green's function as

$$\mathbf{G} = \frac{i}{8\pi^2}\iint \frac{\mathrm{d}k_x \mathrm{d}k_y}{k_z k_1^2} e^{i(k_x x + k_y y + k_z|z|)} \begin{bmatrix} k_1^2 - k_x^2 & -k_x k_y & -+k_x k_z \\ -k_y k_x & k_1^2 - k_y^2 & -+k_y k_z \\ -+k_z k_x & -+k_z k_y & k_1^2 - k_z^2 \end{bmatrix}, \tag{57}$$

where $k_1 = \sqrt{\epsilon_1}k_0$ is the wave-vector magnitude assuming that the emitter is embedded in a medium with permittivity ϵ_1. If the Green's function is known, the optical density of states, ρ_O, may be calculated from

$$\rho_O(\mathbf{r}_0, \omega) = \frac{2\omega}{\pi c^2}\,\mathrm{Im}[\mathrm{Tr}[\mathbf{G}(\mathbf{r}_0, \mathbf{r}_0; \omega)]], \tag{58}$$

where $\mathbf{r}_0$ is the location of the emitter, serving as both the source and observation point.

2.5b. Purcell Factor

The spontaneous emission rate enhancement due to HMMs may be expressed in terms of the Purcell factor, F_P. Assuming spectral and spatial alignment between the emitter (dipole) and modal electric field (mode supported by HMMs), the enhancement may be expressed as

$$F_P = \frac{\Gamma_g}{\Gamma_0}, \tag{59}$$

where

$$\Gamma_0 = \frac{\omega_{21}^3 \mu_{21}^2}{3\pi\epsilon_0 \hbar c^3} \tag{60}$$

is the emission rate in vacuum, and

$$\Gamma_g = \frac{2\pi\mu_{21}^2 E_0^2}{\hbar^2} \rho_O(\omega_{21}) \tag{61}$$

is the emission rate in an environment defined by the frequency-dependent local optical density of states, ρ_O. In Eqs. (60) and (61), ω_{21} is the transition frequency, μ_{21} is the magnitude of the transition dipole moment, and E_0 is the magnitude of the local electric field. In Eq. (61) we assume that the dipole and electric field share the same polarization. Note that if the environment takes the form of a cavity resonant with the dipole, then $\rho_O(\omega_{21}) = (\Delta\omega_{21} V)^{-1}$, where $\Delta\omega_{21} = \omega_{21}/Q$ is the cavity bandwidth and V is the its physical volume [49]. Using the effective modal volume, V_{eff}, the Purcell factor for the cavity becomes

$$F_p = \frac{3\lambda^3 Q}{4\pi^2 V_{\text{eff}}}, \tag{62}$$

where it is assumed that the dipole and cavity mode are spatially and spectrally aligned and share the same polarization.

In spite of low quality factor resonances associated with individual SPPs, an HMM supports a broadband density of states, which may be understood as multiple low effective volume channels, that significantly enhances the rates of dipole emission. Based on the formalism of Subsection 2.5a, the Purcell factor of a randomly oriented dipole, a distance h above a multilayer HMM, is conveniently described as the average of a dipole oriented parallel and normal to the optical axis of the HMM [50]:

$$F_P = \frac{1}{3} F_{P,\perp} + \frac{2}{3} F_{P,\parallel}. \tag{63}$$

The component along the optical axis is governed by the p-polarization reflectivity, r_{1-2}^p, where the subscript denotes the material the radiation is incident from (1) and reflected from (2). The expression is

$$F_{P,\parallel} = 1 - \eta + \eta \frac{3}{2} \operatorname{Im} \int_0^\infty \mathrm{d}k_\perp \frac{k_\perp^3}{w} (1 - r_{1-2}^p) e^{-2ik_{1,\parallel} h}, \tag{64}$$

where $w = -i\sqrt{1 - k_\perp^2}$ and it should be understood that here $k_\perp$ is normalized with respect to k_1.

The component normal to the optical axis depends upon both the p- and s-polarization reflectivity, r_{1-2}^s, through

$$F_{P,\parallel} = 1 - \eta + \eta \frac{3}{4} \mathrm{Im} \int_0^\infty \mathrm{d}k_\perp \frac{k_\perp}{w} [(1 + r^s_{1-2}) - (1 - k_\perp^2)(1 + r^p_{1-2})] e^{-2ik_{1,\parallel}h}. \quad \textbf{(65)}$$

The Fresnel coefficients of an arbitrary multilayer system are explicitly defined in Subsection 2.6a. For a randomly oriented dipole located in the near-field of an HMM, the decay rate is dominated by the high-k channels of the component along the optical axis. For this case the decay rate may be analytically approximated as [8]

$$\Gamma_{\text{high-}k} = \frac{\mu_\perp^2}{8\hbar h^3} \frac{2\sqrt{|\epsilon_\perp|\epsilon_\parallel}}{1 + |\epsilon_\perp|\epsilon_\parallel}, \quad \textbf{(66)}$$

where the effective permittivity elements are defined in Subsection 2.8. The dependence of the second term of Eq. (66) is plotted for a Ag/SiO_2 system in Fig. 5, as a function of wavelength and metal fraction for cases of unperturbed and perturbed constituent oxide. Regions of elliptical and hyperbolic dispersion are denoted by zero and non-zero values of $\mathrm{Im}[r_p] = \sqrt{|\epsilon_\perp|\epsilon_\parallel}/(1 + |\epsilon_\perp|\epsilon_\parallel)$. Maximum Purcell enhancement occurs at the maximum of this quantity. A 10% change in the refractive index of the oxide leads to a dramatic shift in the onset of hyperbolic dispersion and can thus be used to tune the emission rate dynamically.

2.5c. Two Dipoles Near HMM

The case of two dipoles located in the near field of an HMM was recently studied in [48]. The interested reader is suggested to consult this reference for the associated formalism.

2.6. Propagating and Evanescent Waves in Complex Periodic Media

Propagation of electromagnetic plane waves in a one-dimensional periodic system of finite length is exactly described using the transfer matrix method. Under the assumption of infinite periodicity, Bloch's theorem may be invoked, which further simplifies the description of propagating and evanescent waves.

2.6a. Finitely Periodic Systems: The Transfer Matrix Method

The transfer matrix method (TMM) enables the calculation of transmission, reflection, and absorption of plane waves incident at an arbitrary angle onto an arbitrary sequence of infinitely extended layers. Each interface in the multilayer system is described by a

Figure 5

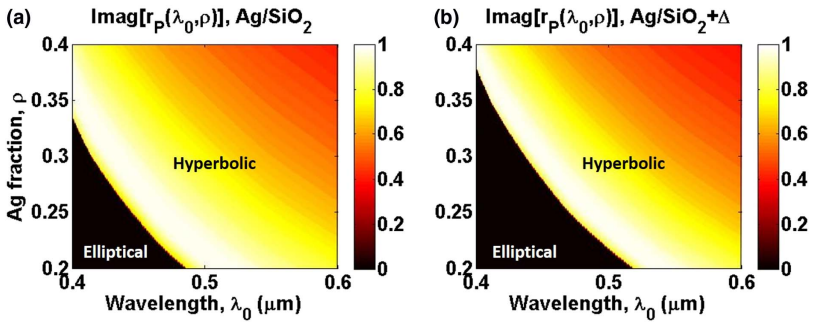

Tuning the near-field Purcell factor via index modulation. Emission enhancement factor, $\mathrm{Im}[r_p] = \sqrt{|\epsilon_\perp|\epsilon_\parallel}/(1 + |\epsilon_\perp|\epsilon_\parallel)$, as a function of vacuum wavelength and Ag fraction in an (a) unperturbed and (b) perturbed Ag/SiO_2 HMM. The refractive index of SiO_2 is 1.5 and $1.5 + \Delta$, $\Delta = 0.15$ in (a) and (b), respectively. The dispersive, complex permittivity of Ag is taken from the literature [51].

transfer matrix and each discrete layer by a propagation matrix. The matrices are cascaded to form a system matrix by which transmission, reflection, and absorption are determined. For completeness, we include a formal description of the TMM based on [52], but expanded in the context of a dynamically variable ϵ or μ.

Generally, the transfer matrix at the interface of materials "1" and "2" may be written as

$$T_{1-2} = \frac{1}{t_{1-2}} \begin{bmatrix} 1 & r_{1-2} \\ r_{1-2} & 1 \end{bmatrix}, \tag{67}$$

where t_{1-2} and r_{1-2} are the, generally complex, transmissivity and reflectivity coefficients for waves coming from material "1" to material "2." Throughout, we describe the direction with respect to the optical axis (which is normal to the layer interfaces). The transfer matrix at a metal–dielectric interface is

$$T_{M-D} = \frac{1}{2\sqrt{\mu_M \mu_D} k_{\parallel,M}} \begin{bmatrix} \mu_M k_{\parallel,D} + \mu_D k_{\parallel,M} & \mu_M k_{\parallel,D} - \mu_D k_{\parallel,M} \\ \mu_M k_{\parallel,D} - \mu_D k_{\parallel,M} & \mu_M k_{\parallel,D} + \mu_D k_{\parallel,M} \end{bmatrix} \tag{68}$$

for TE waves, and

$$T_{M-D} = \frac{1}{2\sqrt{\epsilon_M \epsilon_D} k_{\parallel,M}} \begin{bmatrix} \epsilon_M k_{\parallel,D} + \epsilon_D k_{\parallel,M} & \epsilon_M k_{\parallel,D} - \epsilon_D k_{\parallel,M} \\ \epsilon_M k_{\parallel,D} - \epsilon_D k_{\parallel,M} & \epsilon_M k_{\parallel,D} + \epsilon_D k_{\parallel,M} \end{bmatrix} \tag{69}$$

for TM waves. Equations (68) and (69) explicitly depend on μ and ϵ, respectively, implying that the transfer matrices may be modified by external perturbations through μ and ϵ. Generally, the propagation matrix is independent of polarization and may be written as

$$P_{1-2} = \begin{bmatrix} \exp(i\phi) & 0 \\ 0 & \exp(-i\phi) \end{bmatrix}, \tag{70}$$

where $\phi = k_{\parallel,\alpha} t_\alpha$ is the phase accrued by the wave in traversing the α material of thickness t_α. The component of the wave vector parallel to the optical axis is determined through

$$k_{\parallel,\alpha} = \sqrt{\epsilon_\alpha \mu_\alpha k_0^2 - k_\perp^2}, \tag{71}$$

where $k_\perp$ is normally considered a real-valued, independent variable. Depending upon the value of ϵ_α and μ_α, $k_{\parallel,\alpha}$ may therefore be purely real, purely imaginary, or complex-valued.

For a system of N periods terminated by vacuum on both ends, the system matrix $\mathbf{S}$ is

$$\begin{bmatrix} E_+^0 \\ E_-^0 \end{bmatrix} = \mathbf{S} = T_{0-1}(P_1 T_{1-2} P_2 T_{2-1})^N T_{1-0} \begin{bmatrix} E_+^N \\ E_-^N \end{bmatrix}. \tag{72}$$

The transmission, reflection, and absorption are then computed as

$$T = |t|^2 = \frac{|\mathbf{S}(2,1)|^2}{|\mathbf{S}(1,1)|^2}, \tag{73}$$

$$R = |r|^2 = \frac{1}{|\mathbf{S}(1,1)|^2}, \tag{74}$$

$$A = 1 - T - R. \tag{75}$$

From Eqs. (67)–(75) it becomes clear that external perturbations to ϵ and μ will directly affect the transmission, reflection, and absorption of waves propagating through hyperbolic media.

In principle, the TMM enables the exact determination of transmission, reflection, and absorption in an arbitrary sequence of isotropic materials with complex, and field-dependent, ϵ and μ. However, in practice, the two exponentials in the propagation matrix have opposing sign, leading one to be extremely large while the other is extremely small when lossy materials and evanescent waves are considered. The smaller value will be of the order of the machine precision of most microprocessors, which leads to systemic errors and non-physical results. To remedy this problem, the scattering matrix method [53,54] may be used, which is the subject of the next section.

2.6b. Finitely Periodic Systems: The Scattering Matrix Method

The scattering matrix method (SMM) is an iterative procedure that uses transfer and propagation matrices. Unlike the TMM, however, the propagation matrix of the SMM contains exponential functions whose arguments have the same sign. Consequently, the divergence issues associated with the TMM are eliminated at the expense of higher algorithmic complexity [53,54]. Similar to the TMM, ϵ and μ appear explicitly, providing the means to modify scattering via external control mechanisms. Here we summarized the algorithm of [55] in the context of tunable and active constituent materials.

First, a system matrix is initialized,

$$\mathbf{S_0} = \begin{bmatrix} 0 & 1 \\ 1 & 0 \end{bmatrix}, \tag{76}$$

followed by a propagation matrix,

$$\mathbf{P_0} = \begin{bmatrix} 0 & \exp(ik_{\parallel,0}t_0) \\ \exp(ik_{\parallel,0}t_0) & 0 \end{bmatrix}. \tag{77}$$

The initial system and propagation matrices are fed into the next system matrix $\mathbf{S}$ with the recurrence relation

$$\mathbf{S_{n+1}} = \begin{bmatrix} \mathbf{S_n}(1,1) + \mathbf{S_n}(1,2)\mathbf{Y_n}(1,1)\mathbf{S_n}(2,1)q_n & \mathbf{S_n}(1,2)\mathbf{Y_n}(1,2)q_n \\ \mathbf{Y_n}(2,1)\mathbf{S_n}(2,1)q_n & \mathbf{Y_n}(2,2) + \mathbf{S_n}(2,2)\mathbf{Y_n}(1,2)\mathbf{Y_n}(2,1)q_n \end{bmatrix}, \tag{78}$$

with

$$q_n = \frac{1}{1 - \mathbf{Y_n}(1,1)\mathbf{S_n}(2,2)}. \tag{79}$$

In the above equations, $\mathbf{Y_n}$ may be either a propagation or transfer, i.e., interface, matrix, and the parentheses refer to matrix element row and column. The transfer matrices are defined as

$$T_{0-1} = \frac{1}{\frac{k_{\parallel,0}}{\epsilon_0} + \frac{k_{\parallel,1}}{\epsilon_1}} \begin{bmatrix} \frac{k_{\parallel,0}}{\epsilon_0} - \frac{k_{\parallel,1}}{\epsilon_1} & 2k_{\parallel,1} \\ 2k_{\parallel,0} & \frac{k_{\parallel,1}}{\epsilon_1} - \frac{k_{\parallel,0}}{\epsilon_0} \end{bmatrix}. \tag{80}$$

The system matrix is updated for each additional layer until the final, Nth, layer is reached. Then the intensity transmission, T, reflection, R, and absorption, A, are calculated from the complex amplitude transmissivity, t, and reflectivity, r, by

$$T = |t|^2 = |\mathbf{S_N}(2,1)|^2, \tag{81}$$

$$R = |r|^2 = |\mathbf{S_N}(1,1)|^2, \tag{82}$$

$$A = 1 - T - R, \tag{83}$$

where

$$\mathbf{S_N} = \begin{bmatrix} \mathbf{S_N}(1,1) & \mathbf{S_N}(2,1) \\ \mathbf{S_N}(1,2) & \mathbf{S_N}(2,2) \end{bmatrix}, \tag{84}$$

with

$$\mathbf{S_N}(1,1) = \mathbf{S_{N-1}}(1,1) + \mathbf{S_{N-1}}(1,2)\mathbf{P_{N-1}}(1,1)\mathbf{S_{N-1}}(2,1)q_{N-1}, \tag{85}$$

$$\mathbf{S_N}(2,1) = \mathbf{S_{N-1}}(1,2)\mathbf{Y_n}(1,2)q_{N-1}, \tag{86}$$

$$\mathbf{S_N}(1,2) = \mathbf{P_{N-1}}(2,1)\mathbf{S_{N-1}}(2,1)q_{N-1}, \tag{87}$$

$$\mathbf{S_N}(2,2) = \mathbf{P_{N-1}}(2,2) + \mathbf{S_{N-1}}(2,2)\mathbf{P_{N-1}}(1,2)\mathbf{P_{N-1}}(2,1)q_{N-1}. \tag{88}$$

The SMM was used in the analysis of active multilayer metal–dielectric slabs [37], where propagation through alternating layers of Ag and InGaAsP MQWs was compared with AZO and InGaAsP MQWs. As Fig. 6 shows, despite Ag having a higher intrinsic loss than AZO, the Ag/InGaAsP system is far superior in permitting gain-enhanced transmission. These analytical results were further confirmed by the finite-difference time-domain numerical method [56]. Along with analyses based on the EMA [36], these SMM results encouraged the experimental demonstration of the Ag/InGaAsP MQW platform for active hyperbolic dispersion in the near-infrared [57].

2.6c. Infinitely Periodic Systems: Bloch Theory

In the limit of an infinite number of periods, Bloch's theorem enables the determination of band structure. At a particular wavelength, the relation between components of the wave vector parallel and normal to the optical axis may be determined. This relation is related to the optical DOS and is used in discussing the passive properties of HMMs. For completeness we include the formalism here, based on [58].

In a metamaterial composed of alternating layers of a metal and dielectric, the relative permittivity is a periodic function,

$$\epsilon(z) = \epsilon(z + \Lambda), \tag{89}$$

where $\Lambda = t_M + t_D$ is the one-dimensional lattice period, and we assume the layer interfaces lie in the plane normal to the z-direction. The periodicity of the permittivity is then analogous to the periodicity of the atomic potential in solid-state crystals and electromagnetic wave propagation through the multilayer photonic crystal is analogous to electron wave propagation through an atomic lattice. In the context of solid-state physics, Bloch's theorem states that the eigenfunctions of the one-electron Hamiltonian of an infinite crystal may be expressed as the product of a plane wave and a function with the periodicity of the lattice. Accordingly, the electric field vector

of a normal mode of propagation in the periodic metal–dielectric multilayer may be written as

$$\mathbf{E} = \mathbf{E}_{K_\parallel}(z)\exp(i\omega t - k_\perp x)\exp(-iK_\parallel z), \tag{90}$$

where $K_\parallel$ is the Bloch wavenumber of the system, and

$$\mathbf{E}_{K_\parallel}(z) = \mathbf{E}_{K_\parallel}(z+\Lambda). \tag{91}$$

As was shown in the discussion of the TMM, the electric field within period n of the multilayer may be decomposed into incoming and outgoing fields, E_+^n and E_-^n, respectively. By Bloch's theorem, the fields within the next period are related by

$$\begin{bmatrix} E_+^{n-1} \\ E_-^{n-1} \end{bmatrix} = \exp(iK_\parallel \Lambda)\begin{bmatrix} E_+^{n} \\ E_-^{n} \end{bmatrix}. \tag{92}$$

Using the TMM we can relate the fields in adjacent periods through a matrix of the form

Figure 6

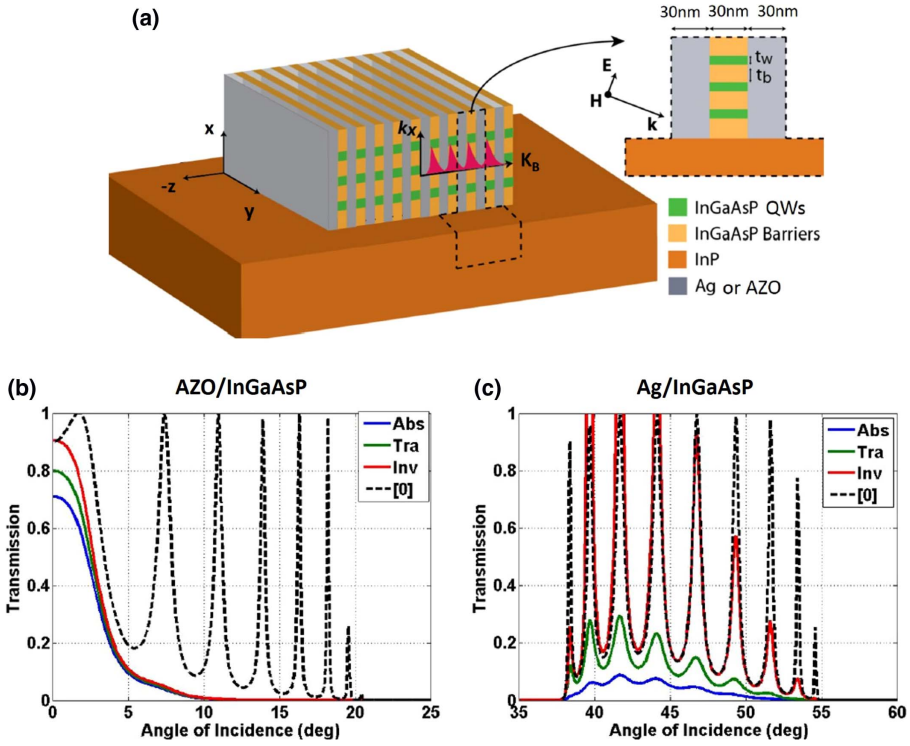

Transmission in active multilayer HMM [37]. (a) Schematic of lateral multilayer consisting of InGaAsP MQW as the active constituent dielectric and either Ag or AZO as the metal. Transmission through multilayer with (b) AZO and (c) Ag calculated according to SMM. In each calculation, the structure consists of 10 periods with 30 nm alternating layers of InGaAsP and metal. Solid blue, green, and red curves correspond to cases when the InGaAsP layers are absorbing, transparent, and active, respectively, while the metal layers are absorbing. Dashed black curves correspond to the hypothetical case when all layers are transparent. The signal wavelength is 1500 nm. Reprinted with permission from [37]. Copyright 2015 Optical Society of America.

$$\begin{bmatrix} A & B \\ C & D \end{bmatrix} = P_1 T_{1-2} P_2 T_{2-1}, \tag{93}$$

such that

$$\begin{bmatrix} E_+^{n-1} \\ E_-^{n-1} \end{bmatrix} = \begin{bmatrix} A & B \\ C & D \end{bmatrix} \begin{bmatrix} E_+^{n} \\ E_-^{n} \end{bmatrix}, \tag{94}$$

where

$$A = \exp(ik_{\parallel,1}t_1)\left[\cos(k_{\parallel,2}t_2) + \frac{i}{2}\left(\frac{k_{\parallel,2}}{k_{\parallel,1}} + \frac{k_{\parallel,1}}{k_{\parallel,2}}\right)\sin(k_{\parallel,2}t_2)\right], \tag{95}$$

$$B = \exp(-ik_{\parallel,1}t_1)\left[\frac{i}{2}\left(\frac{k_{\parallel,2}}{k_{\parallel,1}} - \frac{k_{\parallel,1}}{k_{\parallel,2}}\right)\sin(k_{\parallel,2}t_2)\right], \tag{96}$$

$$C = \exp(ik_{\parallel,1}t_1)\left[-\frac{i}{2}\left(\frac{k_{\parallel,2}}{k_{\parallel,1}} - \frac{k_{\parallel,1}}{k_{\parallel,2}}\right)\sin(k_{\parallel,2}t_2)\right], \tag{97}$$

$$D = \exp(-ik_{\parallel,1}t_1)\left[\cos(k_{\parallel,2}t_2) - \frac{i}{2}\left(\frac{k_{\parallel,2}}{k_{\parallel,1}} + \frac{k_{\parallel,1}}{k_{\parallel,2}}\right)\sin(k_{\parallel,2}t_2)\right] \tag{98}$$

for TE-polarized modes (assuming $\mu = \mu_0$), and

$$A = \exp(ik_{\parallel,1}t_1)\left[\cos(k_{\parallel,2}t_2) + \frac{i}{2}\left(\frac{\epsilon_2 k_{\parallel,1}}{\epsilon_1 k_{\parallel,2}} + \frac{\epsilon_1 k_{\parallel,2}}{\epsilon_2 k_{\parallel,1}}\right)\sin(k_{\parallel,2}t_2)\right], \tag{99}$$

$$B = \exp(-ik_{\parallel,1}t_1)\left[\frac{i}{2}\left(\frac{\epsilon_2 k_{\parallel,1}}{\epsilon_1 k_{\parallel,2}} - \frac{\epsilon_1 k_{\parallel,2}}{\epsilon_2 k_{\parallel,1}}\right)\sin(k_{\parallel,2}t_2)\right], \tag{100}$$

$$C = \exp(ik_{\parallel,1}t_1)\left[-\frac{i}{2}\left(\frac{\epsilon_2 k_{\parallel,1}}{\epsilon_1 k_{\parallel,2}} - \frac{\epsilon_1 k_{\parallel,2}}{\epsilon_2 k_{\parallel,1}}\right)\sin(k_{\parallel,2}t_2)\right], \tag{101}$$

$$D = \exp(-ik_{\parallel,1}t_1)\left[\cos(k_{\parallel,2}t_2) - \frac{i}{2}\left(\frac{\epsilon_2 k_{\parallel,1}}{\epsilon_1 k_{\parallel,2}} + \frac{\epsilon_1 k_{\parallel,2}}{\epsilon_2 k_{\parallel,1}}\right)\sin(k_{\parallel,2}t_2)\right] \tag{102}$$

for TM-polarized modes.

Thus, we establish the eigenvalue problem for the Bloch wave:

$$\begin{bmatrix} A & B \\ C & D \end{bmatrix} \begin{bmatrix} E_+^{n} \\ E_-^{n} \end{bmatrix} = \exp(iK_\parallel \Lambda) \begin{bmatrix} E_+^{n} \\ E_-^{n} \end{bmatrix}. \tag{103}$$

Solving for the eigenvalue, we have

$$\exp(iK_\parallel \Lambda) = \frac{A+D}{2} \pm \sqrt{\frac{(A+D)^2}{2} - 2(AD - BC)}, \tag{104}$$

which is equivalent to

$$\cos(K_{\parallel}\Lambda) = \frac{1}{2}(A + D). \tag{105}$$

The Bloch wavenumber is thus determined as

$$K_{\parallel} = -\frac{1}{\Lambda}\cos^{-1}\left(\frac{A + D}{2}\right) + \frac{2\pi}{\Lambda}s, \ldots s = 0, 1, 2\ldots \tag{106}$$

The complex permittivity of the constituent materials affects $K_{\parallel}$ explicitly in Eqs. (95)–(102). Hence tuning and loss compensation for the Bloch wave is achieved by tuning and providing gain to the constituent materials. Generally, $K_{\parallel} = K'_{\parallel} + iK''_{\parallel}$. In the absence of material loss or gain, $K_{\parallel}$ is either purely real or imaginary, where non-zero values of $K'_{\parallel}$ and $K''_{\parallel}$ describe regions of propagating and evanescent waves in momentum space, respectively. When material loss or gain is present, $K_{\parallel}$ is complex over the entire momentum space (span of $k_{\perp}$), and the separation between propagating and evanescent behavior is less clear. Nonetheless, analyzing Bloch waves in the presence of loss and gain provides useful information on the potential for achieving active HMMs [59]. Even in the absence of loss or gain, Bloch analysis is useful for identifying the angular bandwidth over which a metal–dielectric system transmits high-k states. In Fig. 7, this is done for infinitely periodic multilayers consisting of InGaAsP as the dielectric and either AZO or Ag as the metal. A clear distinction between the two systems is observed. Namely, the range of $k_x = k_{\perp}$ values supported in the AZO system has no minimum but a maximum around $3k_0$, while the range of such values in the Ag system has a minimum and maximum around $5k_0$ and $6.5k_0$, respectively. These traits of the two systems are characteristic of Type I and Type II hyperbolic dispersion, respectively. Dynamically perturbing the constituent materials results in a modification to these values, leading to changes in observables such as transmission (see Fig. 6).

Figure 7

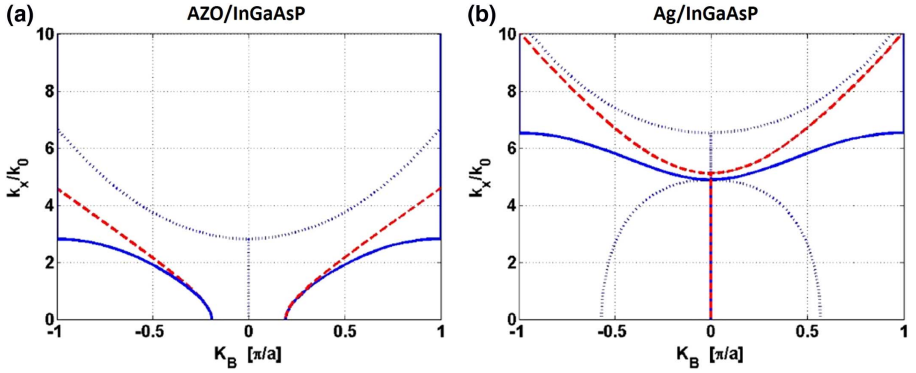

Wave-vector diagrams calculated according to Bloch's theorem [37]. InGaAsP-based multilayer with (a) AZO and (b) Ag as the constituent metals. In each calculation, the structure consists of an infinite number of periods with 30 nm alternating layers of InGaAsP and metal, each modeled as transparent materials. Solid and dashed blue curves correspond to the real and imaginary-valued solutions to Eq. (106), while the red curve is the effective medium approximation detailed in Subsection 2.8. The signal wavelength is 1500 nm. Reprinted with permission from [37]. Copyright 2015 Optical Society of America.

2.7. Effective Medium Theory

2.7a. Dispersion Relation

Effective medium theory reduces the complexity of the complete description of a system of two or more distinct materials [60]. The main assumption of the EMA is that the characteristic length of the system, l_α, is much smaller than the wavelength of the of the electromagnetic wave propagation in the medium, λ_0/n_{eff}, that is,

$$\lambda_0 \ll n_{\text{eff}} l_\alpha, \tag{107}$$

where n_{eff} is the effective index of the mode of interest. This assumption arises from a Taylor series expansion of Eq. (106) and retaining only the lowest-order term. Doing this we obtain polarization-dependent dispersion relations in an anisotropic medium. Using TM and TE polarization to refer to polarization states with electric field in-plane and out-of-plane with respect to the optical axis of the multilayer, respectively, the dispersion relation is [61,62]

$$\frac{\omega^2}{c^2} = k_0^2 = \frac{k_\perp^2}{\epsilon_\parallel \mu_\perp} + \frac{k_\parallel^2}{\epsilon_\perp \mu_\perp} \tag{108}$$

for TM polarization. Solving for the component parallel to the optical axis we see that effective medium theory approximates Bloch's theorem by the substitution of $K_\parallel$ with $k_\parallel$:

$$k_\parallel = \pm\sqrt{\epsilon_\perp\left(k_0^2 - \frac{k_\perp^2}{\epsilon_\parallel}\right)}, \tag{109}$$

where the sign is determined through the causality requirement that $\epsilon_\perp k_\parallel > 0$ [61].

For TE-polarized waves, the effective medium dispersion relation is

$$\frac{\omega^2}{c^2} = k_0^2 = \frac{k_\perp^2}{\epsilon_\perp \mu_\parallel} + \frac{k_\parallel^2}{\epsilon_\perp \mu_\perp}. \tag{110}$$

For wave propagation along the optical axis, the effective index of a mode may be defined as

$$n_{\text{eff}} = \frac{k_\parallel}{k_0}, \tag{111}$$

which, along with λ_0, determines the applicability of the EMA.

According to the zeroth-order, local EMA, the electrical response of the system is described by a diagonal permittivity tensor, $\tilde{\epsilon}$, of the form [60]

$$\tilde{\epsilon} = \epsilon_0 \begin{bmatrix} \epsilon_\perp & 0 & 0 \\ 0 & \epsilon_\perp & 0 \\ 0 & 0 & \epsilon_\parallel \end{bmatrix}. \tag{112}$$

The equivalence of a multilayer metal-dielectric system and an HMM is shown in Figs. 1(a) and 1(b), with the optical axis, **c**, pointing normal to the layer interfaces. In writing Eq. (112), we have assumed TM polarization of the electromagnetic wave, such that the magnetic field points in the direction normal to the optical axis.

To account for possible hyperbolic dispersion for TE polarization, in which the electric field points normal to the optical axis, we describe the magnetic response of the system by an analogous diagonal permeability tensor, $\tilde{\mu}$, of the form [62]

$$\tilde{\mu} = \mu_0 \begin{bmatrix} \mu_\perp & 0 & 0 \\ 0 & \mu_\perp & 0 \\ 0 & 0 & \mu_\parallel \end{bmatrix}, \tag{113}$$

where μ_0 is the vacuum permeability. For a given frequency, Eqs. (112) and (113) generally describe an ellipse when $\epsilon'_\perp \epsilon'_\parallel > 0$ and $\mu'_\perp \mu'_\parallel > 0$, respectively, where the single prime denotes real part. This is the case of conventional anisotropic materials, i.e., dielectric crystals. However, when the orthogonal elements of the permittivity and permeability tensors have opposite sign, Eqs. (112) and (113) describe hyperbolas. Generally, two types of hyperbolic dispersion exist for each polarization, depending upon whether one or two of the effective tensor elements are negative. When one and two of the principal directions are negative, the dispersion is called Type I and Type II, respectively. Types I and II for TM polarization are thus described by $\epsilon_\perp > 0$, $\epsilon_\parallel < 0$ and $\epsilon_\perp < 0$, $\epsilon_\parallel > 0$, respectively.

2.7b. Multilayer Metal–Dielectric System

For a multilayer system of metal fill fraction, $\rho = t_M/\Lambda$, the elements of $\tilde{\epsilon}$, and $\tilde{\mu}$ by appropriate substitution, are [60,61]

$$\epsilon_\perp(\omega) = \epsilon'_\perp(\omega) + i\epsilon''_\perp(\omega, N) = \rho\epsilon_M(\omega) + (1-\rho)\epsilon_D(\omega, N), \tag{114}$$

$$\epsilon_\parallel = \epsilon'_\parallel(\omega) + i\epsilon''_\parallel(\omega, N) = \frac{\epsilon_M(\omega)\epsilon_D(\omega, N)}{\rho\epsilon_D(\omega, N) + (1-\rho)\epsilon_M(\omega)}. \tag{115}$$

In Eqs. (114) and (115), the imaginary permittivity elements are written as an explicit function of the free carrier density, N, discussed in Section 2.3.

2.7c. Nanowire Array System

Similarly, a system composed of an array of metallic nanowires in a dielectric host may be described by a zero-order effective medium approximation. For a nanowire system with radius r_{nw} and lattice constant a_{nw}, the metal fill fraction is $\rho = \frac{\pi r_{nw}^2}{a_{nw}^2}$. Under the assumption that $\rho \leq 0.3$, the effective permittivity elements become [61]

$$\epsilon_\perp = \rho\epsilon_M + (1-\rho)\epsilon_D, \tag{116}$$

$$\epsilon_\parallel = \frac{2\rho\epsilon_M\epsilon_D + (1-\rho)\epsilon_D(\epsilon_M + \epsilon_D)}{2\rho\epsilon_D + (1-\rho)(\epsilon_M + \epsilon_D)}. \tag{117}$$

2.7d. Higher-Order Approximations

Local effective medium theory accounts for only the zero-order term in a Taylor series expansion of the wave-vector-dependent permittivity, which may generally be written as

$$\epsilon_{\perp,\parallel}(k) = \epsilon_{\perp,\parallel}(0) + \sum_i k_i \frac{\partial}{\partial k_i}(\epsilon_{\perp,\parallel}(k))_{k=0} + \sum_{ij} \frac{k_i k_j}{2} \frac{\partial^2}{\partial k_i \partial k_j}(\epsilon_{\perp,\parallel}(k))_{k=0} + \ldots \tag{118}$$

The higher-order terms describe spatial dispersion, or non-local effects, where the responding displacement field occurs at a position distinct from the driving electric field. These effects become more important as the length of the period of the HMM increases with respect to the operating wavelength. If the HMM possesses centro-symmetry, which is often the case, the odd order terms of Eq. (118) vanish. Accounting for the second-order correction, the dispersion becomes

$$k_0^2 = \frac{k_\perp^2}{\epsilon_\parallel + k_\perp^2 \frac{\partial^2 \epsilon_\parallel(k)}{\partial k_\perp^2} + k_\parallel^2 \frac{\partial^2 \epsilon_\parallel(k)}{\partial k_\parallel^2}} + \frac{k_\parallel^2}{\epsilon_\perp + k_\perp^2 \frac{\partial^2 \epsilon_\perp(k)}{\partial k_\perp^2} + k_\parallel^2 \frac{\partial^2 \epsilon_\perp(k)}{\partial k_\parallel^2}} \tag{119}$$

for TM waves, and

$$k_0^2 = \frac{k_\perp^2}{\epsilon_\perp} + \frac{k_\parallel^2}{\epsilon_\perp \left(1 - k_0^2 \frac{\partial^2 \epsilon_\perp(k)}{\partial k_\parallel^2}\right)^{-1}} \tag{120}$$

for TE waves [62]. Alternatively one can substitute the following expressions for the zero-order permittivity elements, which illustrate the explicit dependence on the ratio of HMM periodicity, Λ, to operating wavelength, λ_0 [63]:

$$\epsilon_\perp^{(2)} = \epsilon_\perp^{(0)} + \frac{1}{3}\left[\frac{\Lambda\pi\rho}{\lambda_0}(1-\rho)(\epsilon_m - \epsilon_D)\right]^2, \tag{121}$$

$$\epsilon_\parallel^{(2)} = \epsilon_\parallel^{(0)} + \frac{1}{3}\left[\frac{\Lambda\pi\rho}{\lambda_0}(\epsilon_\parallel^{(0)})^3(1-\rho)\left(\frac{1}{\epsilon_m} - \frac{1}{\epsilon_D}\right)\right]^2. \tag{122}$$

Here, $\epsilon_\perp^{(0)}$ and $\epsilon_\parallel^{(0)}$ are given by Eq. (114) and Eq. (115), respectively. The case of a non-centro-symmetric HMM is discussed in Subsection 5.2b.

2.8. Resonance Cones

Radiation in extremely anisotropic media was first analyzed theoretically in the context of an ionized gas in a static magnetic field [64]. The direction of the magnetic field defined an axis of symmetry, which in the context of crystal optics, we denote as the optical axis, **c**, of a uniaxial medium. (Note that electromagnetic waves polarized in the plane containing **c** experience the anisotropy of the medium and are known as extraordinary, whereas waves polarized normal to **c** experience an isotropic medium and are therefore known as ordinary). Kuehl analyzed the radiation patterns of dipoles situated in the anisotropic media first studied by Bunkin and found that the Poynting vector diverges at particular angles with respect to **c**, leading to an infinite radiation resistance of antennas in a magnetized plasma [65]. While the "infinity catastrophe" was dispelled [66], the highly directional emission of radio waves in magnetized plasmas was eventually experimentally observed [67]. Namely, a resonance cone was first demonstrated by Fisher and Gold in a warm anisotropic plasma probed with a radio frequency electric field. In this experiment the authors applied a static magnetic field along the axis of an Ar plasma column contained on a glass cylinder. With the magnetic field, the plasma becomes anisotropic, and the solution of Maxwell equations results in oscillating dipole electric fields along an axis tilted with respect to the applied magnetic field. The resonance cone angle depends then on the plasma density, magnetic field amplitude, and incident frequency. A consequence is that the Poynting vector is also singular on the resonance cones, together with the power flow.

In anisotropic media the Poynting vector, **S**, and wave vector, **k**, are not parallel. It was shown that **S** in media describable by hyperbolic dispersion exhibit a singularity along a particular direction with respect to the optical axis, **c**. This angle was dubbed the resonance cone angle, θ_{RC}, and is given by the relation [67]

$$\theta_{RC} = \tan^{-1}\sqrt{-\frac{\epsilon_{\perp}}{\epsilon_{\parallel}}}, \tag{123}$$

where the permittivity elements are usually assumed purely real.

In metamaterials, resonance cones were proposed on a planar wire-grid network loaded with capacitors and inductors excited by a localized single-frequency source [68]. In this case, the directions of the zeros in the reactance across the grid surface define the resonance cone direction. The wire-grid network also presents negative reflection and subwavelength focusing. Interchanging the capacitors and inductors results in different impedances of the network that affect the impedance of small RF probe [69]. Double-resonance cones were predicted on multilayer nanostructures described by the EMA [70]. With the use of non-linear metamaterials, not just the fundamental electric field, but also the second-harmonic generated signal will propagate along resonance cones. The resonance cone angle is different due to the higher frequency of the second-harmonic generated signal, allowing subwavelength non-linear microscopy.

More recently, experimental results in a Ag/InGaAsP system demonstrated that, for a dispersive HMM, the propagation loss is also singular along the resonance cone [57]. These results were used to show that, in the case of HMMs presenting gain, shorter wavelengths are more likely to be detected because they propagate closer to the metacrystal axis and therefore experience less attenuation than longer wavelengths. The dispersion of the effective permittivity of the Ag/InGaAs system is shown in Fig. 8, along with the dispersion of the resonance cone angle and its visualization. Over the wavelength range in which the constituent dielectric becomes active, the system exhibits Type II hyperbolic dispersion. The resonance cone angle is an increasing function of wavelength. It was hypothesized that the latter relationship leads to a blueshifting of InGaAs emission under external pumping [57]. Blueshifting of emission was similarly observed in an active HMM based on organic dyes, with the effect being attributed to the Purcell effect [71].

3. EXPERIMENTAL EFFECTS

3.1. Broadband Purcell Effect

3.1a. Emitters Near and Inside HMM

Light emission is inherently an active process, in that light emission from a system occurs, whether spontaneous or stimulated, only by the injection of energy into the system from an external source such that the ground state of the system is unoccupied. A direct consequence of the large photonic density of states of HMMs is an enhanced decay rate of quantum emitters in the vicinity of the HMM, relative to vacuum. Furthermore, unlike conventional plasmonic structures based on resonant enhancement, enhancement in HMMs is broadband and passively or actively tunable depending on the ratio of metal to dielectric constituent materials.

One of the major applications of active HMMs is the broadband enhancement of spontaneous emission, which could lead to high-speed, high-efficiency light-emitting diodes (LEDs) and to efficient single-photon sources [72] (see Subsection 4.1). This is achieved through the simultaneous increase in the rate and intensity of spontaneous

emission from quantum emitters (dye molecules, quantum dots, nitrogen vacancy centers, quantum wells, etc.) located within or adjacent to HMMs.

In addition to rate and intensity enhancement of light emitters near and within the HMM, the directionality and polarization of emission can be controlled with HMMs [57,73–75]. Control of the emission direction and polarization has obvious applications for directive illumination and communications. By combining the inherent directional and polarization-sensitive emission of passive HMMs with external tuning mechanisms, beam-forming becomes possible, which would be instrumental for visible light communication systems and LIDAR, for example. HMMs that modify the emission rate, intensity, polarization, or direction are summarized in Fig. 9.

HMMs themselves are also highly tailorable sources of directional thermal radiation [62]. The thermal emission spectrum of HMMs can be engineered for enhancement or suppression of thermal radiation, which makes them excellent candidates as components of thermophotovoltaic systems [76].

3.1b. Thermal Emission of HMMs

A heat source emanates propagating waves whose energy is carried away to the far field. This energy dictates the upper limit for the blackbody emission but it is not a fundamental limit since evanescent waves enable energy transport in the near field. The power, P, irradiated from a unit surface of a body in free space per unit interval of frequency is non-coherent, isotropic, and given by

$$P(\omega) = \frac{hbar\omega^3 e_s(\omega)}{4\pi^2 c^2} \exp\left(\frac{-\hbar\omega}{k_B T_s}\right), \tag{124}$$

where T_s is the temperature of the body surface and $e_s(\omega)$ is the spectral emissivity of the body's material. In the classical theory of thermal radiation, an emitting body can have the maximal thermal radiation emitted if $e_s(\omega) = 1$ and it is considered a transparent media with absent emission if $e_s(\omega) = 0$, when no optical losses are considered at the specific frequency. Absorption is reciprocal to emission.

Once evanescent waves are considered, there is energy transport in the near field, and thermal radiation beyond the blackbody limit is possible. The phenomenon relies on the enhanced density of photonic states of surface electromagnetic states [77] and edges of photonic crystals bandgaps [78], being limited by a narrow bandwidth.

HMMs allow the propagation of bulk plasmon polariton modes with high-k that contributes to the enhancement of the photonic density of states. As a consequence of the broadband Purcell effect in HMMs, emission of thermal radiation from HMMs is enhanced, in addition to emission from dipole sources located within and nearby HMM surfaces. Because the Planck distribution of a thermal body includes only far-field effects while the near-field emission of HMMs is enhanced, the thermal emission of HMMs is considered super-Planckian and non-resonant, not being limited by a narrow bandwidth [79,80].

A demonstration of super-Planckian thermal emission with HMMs was predicted [81] with a metal–dielectric structure composed of SiC and SiO_2. SiC supports SPhP with real part of the permittivity negative in the Reststrahlen band, enabling thermal excitation at temperatures from 400 to 500 K. In the sequence, the same authors proposed the super-Planckian heat transfer in the near field between HMMs composed of plasmonic materials with high melting point [80]. These works pave the way for novel thermophotovoltaic devices for thermal management at the nanoscale [82], including directive thermal emissions in the far-field zone [83], cooled down super-emitters, and so-called thermal black holes [84].

3.1c. Outcoupling Emission

As described in the previous sections, the large photonic density of states supported by HMMs leads to a broadband Purcell effect, which enhances the emission dynamics of dipoles interacting with the HMM, as well as the thermal emission of the HMM itself. While a key signature of this enhancement is a reduced lifetime, a common consequence is a reduced external quantum efficiency because of impedance mismatching between the HMM states and the surrounding vacuum. This problem is common to many plasmonic systems and arises due to the requirement of momentum conservation. Solutions to this problem include gratings, photonic hypercrystals (PHCs), and side-coupling, which have been experimentally demonstrated by numerous groups.

One of the first successful attempts of improved outcoupling was realized with a nanopatterned HMM made of Ag and Si multilayers [9]. The multilayers were patterned with a focused ion beam to form trenches and all covered with rhodamine dye. The covered HMMs were pumped with a 100 fs, 800 nm wavelength laser and visible emission due to two-photon absorption was collected for a time-resolved photoluminescence experiment. The authors reported an intensity enhancement of 76 times compared to rhodamine over a silver substrate. This work created different perspectives toward designing efficient outcoupling for HMMs, and was complemented by work on two-dimensional gratings [85,86].

Figure 8

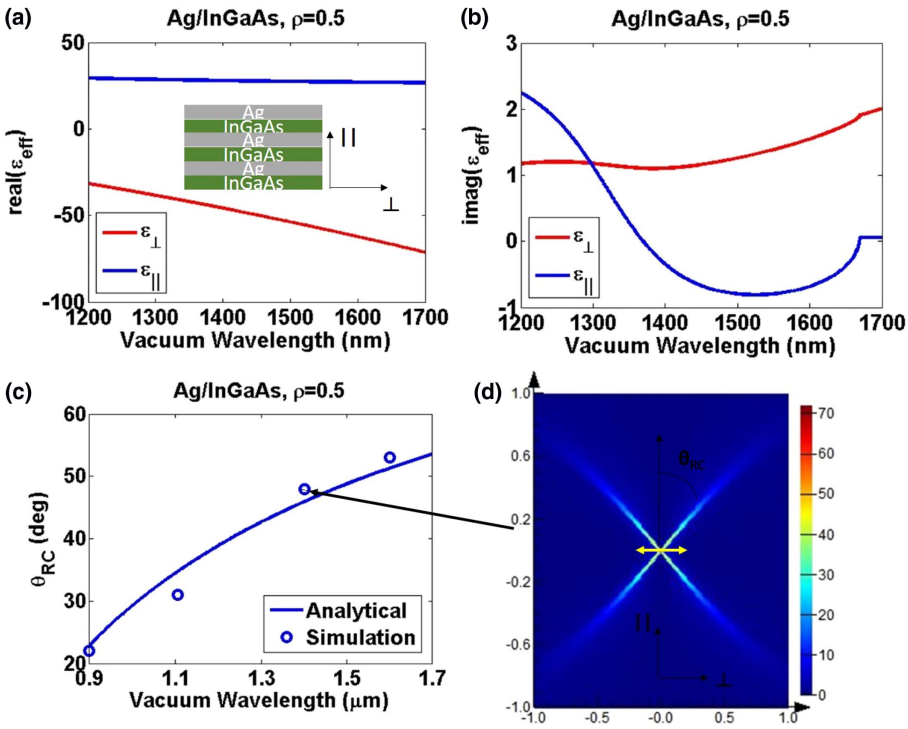

Dispersion and resonance cone of the active Ag/InGaAs HMM under the EMA. (a) Real and (b) imaginary effective permittivity elements as a function of wavelength. Fill fraction and InGaAs carrier density are $\rho = 0.5$ and $N = 5.8 \times 10^{18}$ cm^{-3}, respectively. (c) Resonance cone angle, calculated analytically via Eq. (123) and determined through numerical simulation for $\rho = 0.5$ and purely real permittivity elements. (d) 2D plot of Poynting vector, $S(x, z)$, resulting from numerical simulation at the vacuum wavelength of 1400 nm (axis labels are in units of μm, color is in units of W m^{-2}). The optical axis is in the vertical direction.

Later, more elaborate designs were demonstrated, as a high-index, Ge bullseye grating for efficient outcoupling of the high-k modes with simultaneous spontaneous emission lifetime enhancement [74]. The evanescent modes were excited by quantum dots embedded into an inner layer of the HMM. The authors observed a 10 times lifetime reduction and 20 times larger intensity into a resonant cone.

An interesting follow-up of this work is the use of a so-called photonic hypercrystal [87] to achieve a 20× enhanced radiative rate with a 100× more efficient light outcoupling, again from probed quantum dots inserted within the HMM [88]. A PHC has a large density of states provided by the HMM but with efficient light-scattering provided by a hexagonal grating formed atop the HMM. The same concept of a PHC was used before to enhance the spontaneous emission of transition metal dichalcogenides (TMDs), bi-dimensional materials placed atop the device [89]. Such a work shows the versatility of HMMs that are now being applied to novel material platforms.

Even with the significant amount of work for efficient outcoupling, there is much to be done since all designs are not only material dependent, but also rely on the ratio between the HMM constituents. Tuning the fill fraction to permit efficient side-coupling was recently predicted through a systematic analysis [75] and shown experimentally in active hyperbolic metasurfaces [57,90]. Essentially, side-coupling requires conservation of the wave-vector component orthogonal to that required for top-coupling.

Figure 9

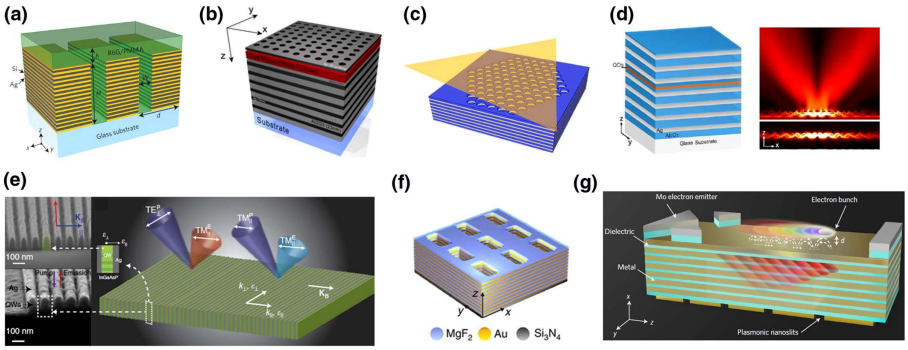

Active HMM for controlling light emission. (a), (b) Dye molecules (a) surrounding [9] and (b) atop [85] multilayer HMM with gratings and (c) monolayer 2D material atop multilayer HMM with grating [89] experience enhancement of spontaneous emission intensity and rate. (d) Quantum dot embedded in center of multilayer HMM with grating experiences directional emission [74]. (e) Quantum wells embedded in lateral multilayer HMM absorb and emit linearly polarized light [57]. (f) Multilayer fishnet HMM exhibits polarization-insensitive directional thermal emission [62]. (g) Flying electrons traveling over multilayer HMM emit visible Cherenkov radiation [91]. (a) Reprinted by permission from Macmillan Publishers Ltd.: Lu *et al.*, Nat. Nanotechnol. **9**, 48–53 (2014) [9]. Copyright 2014. (b) Reprinted by permission from Macmillan Publishers Ltd.: Sreekanth *et al.*, Sci. Rep. **4**, 6340 (2014) [85]. Copyright 2014. (c) Reprinted with permission from Galfsky *et al.*, Nano Lett. **16**, 4940–4945 (2016) [89]. Copyright 2016 American Chemical Society. (d) Reprinted with permission from [74]. Copyright 2015 Optical Society of America. (e) Reproduced from [62] under the terms of the Creative Commons Attribution 4.0 International License. With copyright permission. (f) Reproduced from [57] under the terms of the Creative Commons Attribution 4.0 International License. With copyright permission. (g) Reprinted by permission from Macmillan Publishers Ltd.: Liu *et al.*, Nat. Photonics **11**, 289–292 (2017) [91]. Copyright 2017.

In the Type II regime of multilayer HMMs, the component normal to the optical axis needs to be conserved but it has a lower cutoff, which prevents coupling to vacuum in the absence of a grating. However, side-coupling requires conservation of the wavevector component parallel to the optical axis, which does not have a lower cutoff. Hence coupling to vacuum is achieved without recourse to a grating.

3.2. Hyperimaging and Focusing

Aside from modification to the rate and intensity of spontaneous emission, the transmission of near-field information is one of the most prominent functions of HMMs.

Initial simulation of the far-field hyperlens suggested that sub-100 nm resolution was possible using an illumination wavelength of 365 nm [92]. The first experimental demonstration used this wavelength and achieved 150 nm resolution in one dimension using a cylindrical lens geometry [6,7]. Subsequent work achieved 150 nm resolution in two dimensions using a spherical geometry and a slightly longer working wavelength of 410 nm [93]. More recently, a non-resonant hyperlens was demonstrated achieving 250 nm resolution by using a longer wavelength of 780 nm and a pie-slice geometry [94]. Finally, an array of spherical hyperlenses made by nanoimprint lithography achieved 160 nm resolution at a wavelength of 410 nm [95]. The latter device shows promise for practical application because the design and fabrication circumvent the need for precise placement of the nanoscale objects to be imaged. The resolution performance of the hyperlens is summarized in Fig. 10, with a 10 nm spatial resolution target highlighted for the 365 nm wavelength.

While impressive, hyperlenses have much room for improvement. It is clear that the demonstrated hyperlenses to date are far from sub-10 nm resolution, which is important for real-time imaging in biological and material sciences. In Subsections 4.2a and 4.2b we explore how combining active or tunable components may aid in achieving this goal with a loss-compensated hyperlens and hyperstructured illumination microscopy, respectively.

3.3. Plasmonic Spin Hall Effect

The photonic spin Hall effect describes the phenomenon of circularly polarized light of different handedness propagating along different directions in space. It is a physical analog of the electron spin Hall effect in which electrons of opposing spin traverse different spatial paths under the influence of an external magnetic field. HMMs make excellent platforms for studying and manipulating the photonic spin Hall effect, which due to its plasmonic nature in HMMs, is called the plasmonic spin Hall effect [90].

The spin Hall effect occurs due to the spin polarization-dependent transverse currents originated from the relativistic spin-orbit coupling of electrons. The same effect can be observed with photons, the plasmonic spin Hall effect, and was first observed in a conventional metasurface [96].The analogy of a spin-orbit coupling with a propagating electromagnetic wave is the coupling between the TM and TE fields; however, the interaction is extremely weak and hard to observe. A metasurface was used to control the geometric phase of an incident light beam, leading to a rapidly varying in-plane phase retardation that introduced the strong spin-orbit-like interaction. The effect was observed because of a resonance-induced anomalous “skew scattering” that breaks the axial symmetry of the system, i.e., creates a phase discontinuity.

HMMs were proven to be a natural way of probing the spin Hall effect since the structured interfaces present phase discontinuities that break the symmetry of propagating electromagnetic fields. A two-dimensional RF transmission line metamaterial composed of lumped elements excited by a circular polarized dipole was used to probe the directional routing effect [97]. The system has an anisotropic hyperbolic

dispersion that controls the directionality of energy propagation. In this case, extraordinary modes that exhibit a higher density of states are more strongly localized.

The polarization- and wavelength-dependent routing of surface plasmon polaritons and two-dimensional chiral photons were observed with nanostructured HMMs [90,98]. A deeply subwavelength silver/air grating was used to support SPPs propagating both parallel and perpendicular to the silver ridges, i.e., enabling SPPs with circular polarization. In this case the group velocity changes when moving from the hyperbolic to the elliptical polarization. While a one-dimensional waveguide was used, this demonstration paves the way toward topologically protected plasmonic integrated circuits.

3.4. Cherenkov Radiation

A charged particle crossing a medium with a speed greater than the phase velocity of light in that medium emits electromagnetic radiation, called Cherenkov radiation [99]. If a material exhibits a negative index of refraction, it is possible to generate reverse-Cherenkov radiation, where the particle radiates progressively through the material [100]. The conical radiation wavefront angle is given by

$$\cos\zeta = \frac{\phi}{v} = \frac{c}{nv}, \tag{125}$$

where ϕ is the phase velocity of electromagnetic radiation and v is the particle velocity, both in the guiding medium with refractive index n. If the guiding medium has a negative refraction index, then Eq. (125) predicts the backward propagation of radiation. Depending on their constituent materials and filling ratio, HMMs can generate both forward- and backward-propagating Cherenkov radiation, which was first predicted by Veseslago [101]. One of the first experimental demonstrations of Cherenkov radiation with metamaterials was reported by Grbic and Eleftheriades [102]. To achieve negative permittivity and permeability the authors considered an array of straight conducting wires combined with split-ring resonators, respectively. The metamaterial enables the propagation of an electromagnetic field with negative propagation constant and positive group velocity, resulting in anti-parallel energy flow and phase velocity. In order to achieve more efficient Cherenkov radiation from split-ring resonator-based metamaterials, Xi *et al.* proposed a left-handed metamaterial [103] while

Figure 10

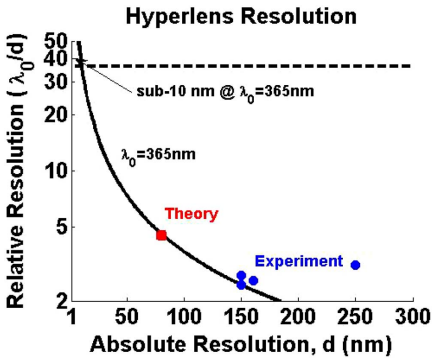

Performance of hyperlens imaging systems to date. Relative and absolute resolution achieved experimentally remains less than that predicted by theory and significantly lower than the 10 nm regime, which would create new possibilities for real-time imaging of interfacial cellular and chemical dynamics.

Duan *et al.* proposed a square waveguide loaded with complementary electric split-ring resonators [104]. In the second case, the authors demonstrated, for the first time, the reverse-Cherenkov radiation. The results were obtained with an all-metal metamaterial, with real charged particles from a single sheet electron beam bunch. The most recent experimental observation of Cherenkov radiation from metamaterials is from Liu *et al.* [91]. Using an integrated HMM formed by alternating Au (70 nm) and SiO_2 (40 nm) thin films, Cherenkov radiation was observed with low electron energies (low electron velocities in the medium) generated from Mo electrodes atop the HMM. The experiment is claimed to be the first realization of an integrated free electron source, enabling a new avenue of applications for HMMs.

3.5. Wave Mixing

Wave mixing is a non-linear optical phenomenon extensively used for ultrashort pulse generation, ultrafast optical switching, and wavelength conversion. Unfortunately, it is a weak process that usually requires phase matching between the different harmonic fields involved. HMMs arise as an unprecedented material for realization of non-linear optics [3,105]. The larger Purcell factor that arises from electromagnetic field localization in the near field can significantly enhance the efficiency of non-linear processes. The interfaces of HMMs can result in symmetry breaking that can enhance metal surface non-linearities. On the other hand, an HMM can benefit from non-linear effects. Its properties are highly dependent on the constituent material permittivities, being tunable with slight modifications, even if generated by high-order non-linear processes [106].

HMMs also afford a hyperbolic dispersion that allows large refractive indices and opportunities to achieve the quasi-phase-matching condition with a wide range of material parameters [107], enabling the formation of double-resonance cones due to a predicted second-harmonic generated electromagnetic field [70]. Further, the negative group velocity of a mode supported by a HMM waveguide can provide a backward-propagating second-harmonic generated signal [108]. The use of HMMs on non-linear optics has opened new avenues, for example, as an integrated source of a paired photon-plasmon through spontaneous wave mixing [109]. These interdisciplinary results strongly suggest that non-linear quantum effects will emerge in HMMs.

4. APPLICATIONS

4.1. High-Speed, High-Efficiency Light Sources

In Subsection 4.1 we reviewed the progress in increasing both the rate and intensity of emitters located in proximity to HMMs. A major potential application leveraging this progress is high-speed, high-efficiency LEDs (here we use "device" rather than "diode" for sake of generality). LEDs with high speeds and high efficiency are essential components to future light-based communication systems [110]. The information handling capacity of HMM-based light sources can be described through the 3 dB bandwidth, $f_{3\,\mathrm{dB}}$. This quantity describes the direct modulation frequency at which the output power of the HMM-LED drops to half its peak value. For an LED with speed limited by the carrier lifetime,

$$f_{3\,\mathrm{dB}} = \frac{1}{2\pi\tau}. \tag{126}$$

From Subsection 4.1 we saw that $\tau < 100$ ps routinely for emitters coupled to HMMs. Therefore, HMM-based LEDs with $f_{3\,\mathrm{dB}} > 1$ GHz are currently feasible and reaching the 10–100 GHz regime is feasible. While the relation between the data transmission rate and modulation bandwidth depends on the modulation format, assuming a 1-to-1

correspondence, then incoherent communication systems based on HMM LEDs with 100 Gbs^{-1} rates on a single channel appear feasible.

Beyond photon sources enabled by spontaneous emission, HMMs can serve as sources of Cherenkov radiation emitted by free electrons [91]. Typically, free electron sources must break a velocity threshold to emit Cherenkov radiation, requiring high energies and macroscopic distances to accelerate to the requisite velocity. However, use of an HMM enables low-energy flying electrons to emit Cherenkov radiation without a velocity threshold [91]. Thus, HMMs provide a chip-scale platform for studying the fundamental interaction of flying electrons with artificial nanostructures, the technological applications of which remain open to the imagination. For instance, if a suitable HMM were used, it may be possible to generate highly direction radiation spanning the infrared to x-ray regimes in a single table-top platform [111].

4.2. Imaging and Focusing of Light with Super Resolution

4.2a. Active Hyperlens

Numerous theoretical studies have considered using organic dyes for visible wavelengths to improve resolving or focusing ability of HMMs. Ni *et al.* considered gain provided by a saturated dye in an HMM based on Ag and a low-index dielectric akin to SiO_2, which exhibits Type II hyperbolic dispersion [112]. Various analytical techniques were compared using the EMA, non-local EMA, Bloch's theorem, and Fourier modal analysis. For modes propagating normal to the plane of the layers, complete loss compensation was deemed feasible under realistic gain conditions, whereas modes propagating in the plane required unphysical gain levels. Additionally, simulations predicted that gain could improve the resolution of subdiffraction-limited imaging devices and provide for a smaller phase variation in epsilon-near-zero transmission devices. Dye-doped low-index dielectrics in combination with Ag were also analyzed by Agryopolus *et al.* [106]. Using the TMM, factor of 2 improvements in transmission of negatively refracting waves were predicted, but full loss compensation was deemed impractical. Savelev *et al.* invoked Bloch's theorem to analyze generic MD systems, again resembling Ag and a low-index dielectric with dye as the gain media [113]. Full loss compensation was predicted for high-k waves propagating normal to the plane of the layers, useful for improved subdiffraction-limited imaging. The potential existence of convective instabilities associated with amplified spontaneous emission was also revealed, which could be harmful for practical applications. Savelev *et al.* later used TMM to look at similar MD systems with a finite number of periods [114]. It was shown that modest transmission improvements were feasible; however, it was predicted that the Purcell effect, i.e., enhanced spontaneous emission rates near the plasma frequency of silver, would degrade the effect of loss compensation. Smalley *et al.* investigated the Ag/InGaAsP system and found that amplification for near-infrared waves propagating along the optical axis was feasible using both the effective medium approximation [36] and the scattering matrix method [37].

A major inspiration for the field of HMMs arose more than a decade ago with the theoretical prediction [92] and experimental demonstration [6,7] of far-field imaging with resolution beyond the Abbe diffraction limit. Ultimately, however, experimental results in hyperimaging have been limited by propagation losses incurred by the high-k components that carry near-field information from the object to the image plane. Numerous numerical studies have suggested that compensating losses with optical gain could enable significantly better resolution in hyperimaging systems, which are of great potential impact to real-time imaging of biomedical specimens. Here we provide a fundamental analysis that may offer additional guidance towards the demonstration of active hyperimaging enhanced by optical gain.

Figure 11 shows a schematic of a five-period Ag/Al_2O_3 (10 nm/20 nm) multilayer that supports propagating high-k modes. A plane wave is launched across the structure and the transmission at red, green, and blue wavelengths is compared for when the Al_2O_3 layers are modeled as passive or as active, with a linear gain coefficient of 3000 cm^{-1}. Improved transmission is evident, especially for longer wavelengths where the ratio of material gain to silver loss is greatest. Importantly, the transmission of higher-order resonances in the presence of gain can match the transmission of lower-order resonances in the absence of gain. Hence it appears feasible that the use of active materials could improve the resolution of hyperimaging systems. Practically, the gain in the calculated system could be implemented by co-sputtering rare-earth ions and oxides and using an optical pump beam in conjunction with a bandpass filter.

4.2b. Hyperstructured Illumination Microscopy

A major drawback of the hyperlens concept is the requirement for a curved geometry and a desired large ratio between inner and outer total structure radii for large magnification [115]. The curved geometry prevents the use of ultrathin films and the large outer radius leads to low transmission efficiency. In response to these challenges, hyperstructured illumination microscopy (HSIM) was proposed [116]. HSIM utilizes the unique dispersive properties of HMMs to scan subwavelength objects. Conventional imaging optics are used to capture the scattered light from the objects and a reconstruction algorithm is used to predict the object permittivity profile that caused the scattering. It is inspired by structured illumination microscopy [117], which originally doubled the resolution of confocal microscopy, and has since become a successful super-resolution imaging technique. In HSIM, the ultimate spatial resolution is limited by the periodicity of the HMM, which can approach 1 nm for a period composed of epitaxially grown materials. Because the geometry is flat, achieving ultrathin multilayer films is much more practical compared to the hyperlens. Further, the total structure can be much thinner than in the hyperlens geometry, with the required thickness determined by the extent of lateral scanning needed to illuminate the entire object.

HSIM is inherently an active process, as the key ingredient, in addition to the HMM, is a tunable-wavelength point source. This is achieved by generating a subwavelength defect in the underside of the HMM, usually milled by a focus ion beam. Monochromatic plane wave light illuminates the defect causing scattering of light inside the HMM. Within the HMM, light of a particular wavelength propagates along a specific direction determined by the resonance cone angle, as detailed in Section 2.8. If an object to be analyzed is placed on the HMM opposite the defect, its permittivity profile can be scanned by changing the wavelength of the plane wave illumination. For example, tuning the wavelength from 425 nm to 750 nm in a Ag/SiO_2 HMM with a 50% fill fraction will scan the beam from approximately 45–70 deg from normal, which translates into scanning the object of interest laterally to an extent depending on the total HMM thickness [116]. HSIM has been shown to be relatively immune to fabrication imperfections, such as interfacial roughness and layer thickness variation within the multilayer HMM [118]. Due to its simplicity relative to hyperlens technology, HSIM shows promise for combining the high-k propagation of hyperbolic media with a tunable light source for super-resolution imaging at visible and infrared wavelengths [119]. The major potential advantage of HSIM over other super-resolution platforms, such as stochastic optical reconstruction microscopy or photo-activated localization microscopy [120], is significantly better temporal resolution. Unlike localization-based techniques, which require buildup of a sufficient photon count to generate an image, HSIM is a "one-shot" process, the temporal resolution of which

is limited only by the speed of numerical reconstruction. It is therefore hoped that HSIM will reveal real-time or video-rate dynamics in the biological and material sciences with spatial resolutions of the order of 10 nm.

4.3. Electro-Optical and All-Optical Modulators

Light propagation is typically considered a passive phenomenon inasmuch as the guiding material is passive. The amplitude and phase of propagating light can be manipulated by passive elements, such as absorption losses and lenses, respectively, but it may also be controlled by active elements. Waveguides made of HMM cores and claddings offer unusual propagation characteristics [121–125], including single-mode higher-order propagation [124] and asymmetric transmission [125] in reciprocal media. With active control, these unusual characteristics become more applicable. For example, the modal dispersion can be controlled in subwavelength waveguides by an external bias [126]. Because HMM waveguides can be extremely compact relative to diffraction-limited waveguides, controlling the dispersion [124] and loss [36] plays an important role to their utility. HMMs can serve as critical elements of integrated electro-optical and all-optical switches for high-speed communications, or even computing [11,25,127]. Additionally, due to strong electric-field enhancement, HMMs function as efficient elements for second-harmonic generation, an important application of which is biomedical sensing [128]. Electro-optical and all-optical modulation enabled by HMMs is summarized in Fig. 12.

4.4. Perfect Absorbers and Thermophotovoltaics

As described by the Shockley Queisser limit [129], the efficiency of a silicon single junction solar cell is limited to less than 35%. The majority of the inefficiency is due to

Figure 11

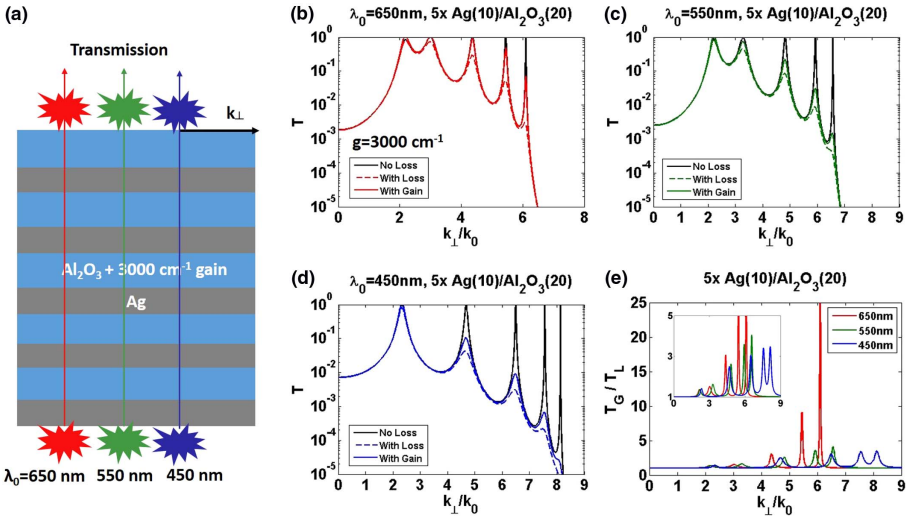

Loss compensation via gain for high-k, visible frequency waves. (a) Schematic of transmission through a five-period Ag/Al_2O_3 (10 nm/20 nm layer thicknesses) multilayer wherein the oxide layer contains 3000 cm^{-1} of material gain. (b)–(d) High-k angular transmission spectra at (b) red, (c) green, (d) blue wavelengths for the cases of a hypothetical zero loss-gain system (black curves), lossy system without gain (dashed curves of color), and lossy system with gain (solid curves of color). (e) Transmission in the lossy system with gain relative to the lossy system without gain. The red and blue wavelengths exhibit greatest and least transmission, because the Ag loss is inversely proportional to wavelength in the visible regime.

spectral losses since photons with energy larger than the semiconductor bandgap lose a portion of their energy to heat and photons below the bandgap are transparent to the cell. On the other hand, thermophotovoltaics (TPV) can overcome the Shockley Queisser limit to achieve theoretical efficiencies greater than 80%. A TPV system concentrates sunlight onto an absorber, transforming the broadband energy spectrum into heat. Next the generated heat is directed at a solar cell using a thermal emitter. The solar cell is typically made of InGaAs with a bandgap near 2100 nm. The main advantage is that the emitter can be engineered to have a narrowband emission spectrum where the internal quantum efficiency of the cell is greatest, drastically reducing spectral losses. Early designs focused on photovoltaic cell materials, solar concentrators, and improved cooling mechanisms that resulted in total efficiencies below 1% [130]. A resurgence of TPV research has recently occurred, fueled mainly by improvements in the selective emitter. However, experimental efficiencies remain less than 4% efficient [131].

Following Kirchoff's law of thermal radiation, the absorption of a material is proportional to its emissivity. HMMs are a good candidate for both emitters and absorbers since they display selective and near-perfect absorption close to the zero-crossing point of their real permittivity. Moreover, the working spectral range can be sufficiently tuned by adjusting the filling fraction. Because the free-space impedance is fixed, however, impedance matching with between air and NIR HMM based on noble metals can be challenging, as both ϵ' and ϵ'' are large in magnitude. Therefore, low-loss metal components with epsilon near zero points within the shortwave IR spectrum (1–3 μm) are being considered for the metallic components of the HMM emitters. Additionally, the desired operating temperature of a TPV emitter is $> 1000^{\circ}$C, which eliminates many low melting point materials, such as noble metals.

Due to the high melting point and appropriate permittivity values, AZO/ZnO-based HMMs are being considered for the emitter component of TPV systems [22,132,133]. It has been reported that by tailoring the parameters of AZO/ZnO HMMs, narrowband emitters can be fabricated to provide theoretical efficiencies that surpass the Shockley Queisser limit [134]. AZO/ZnO multilayers were shown to exhibit negative refraction in the near-infrared, confirming their hyperbolic character [22]. By utilizing a novel fabrication approach, an array of cylindrical AZO/ZnO multilayers was shown to exhibit greater than 85% absorption over the 1200–2200 nm wavelength range, with low sensitivity to angle and polarization [133]. The behavior of the system was described in terms of a photonic hypercrystal [87], which supports even more modes than a conventional multilayer, thus increasing the absorption efficiency. Significantly, the system was shown to be transferable to a flexible substrate and is easily passively tuned by varying geometric parameters [133]. Active tuning of this system via electrical gating should be readily feasible.

5. OUTLOOK

In this section we shift our focus to nascent proposals and experiments on active and tunable HMMs. This includes 2D HMMs, non-reciprocal HMMs, and dipole–dipole interactions in HMMs. While some of the work has been realized, much of it remains to be demonstrated. As such, this section constitutes an outlook on future developments in the field.

5.1. 2D Materials

Graphene behaves as a metal for frequencies in the infrared, with a two-dimensional free electron response for carriers in the lattice plane. Multilayer graphene, for example, graphene layers separated by subwavelength gaps of a dielectric, typically

exhibits Type II hyperbolic dispersion for long wavelengths, with metallic and dielectric response parallel and normal to the lattice plane [135]. Because the chemical potential of graphene is easily controlled by an external bias, per Eq. (16), the electrical conductivity, and therefore the optical response, of graphene exhibits a highly tunable behavior useful for controlling hyperbolic dispersion [136].

Heterostructures made of graphene and hexagonal boron nitride (h-BN) exhibited hybrid plasmon–phonon polaritons with properties dependent on an applied voltage [137]. h-BN is itself a natural HMM [45] that has been shown to exhibit superresolution focusing at mid-infrared wavelengths [138]. The integration of h-BN, and other natural HMMs, with graphene will likely spawn a new class of tunable HMM devices for dynamically controlling mid-infrared light generation, propagation, and absorption.

Simultaneous active and tunable behavior was studied analytically in a multilayer HMM consisting of graphene and thulium-doped silica [139]. Highly tunable, spectrally narrow peaks in the optical gain were predicted for waves polarized such that the optical response was metallic. This corresponds to directions normal and parallel to the graphene plane for Type I (near-infrared) and Type II (mid- to far-infrared) hyperbolic dispersion regimes. The magnitude of gain predicted in the narrow peaks was significantly greater than the broadband gain of the constituent thulium-doped silica. An electromagnetic transparency region was also predicted where absorption becomes vanishingly small by proper external tuning. For waves polarized such that optical response was dielectric, the effect of tuning was negligible and the behavior was similar to the bulk material. This study opens an interesting question into utilizing an

Figure 12

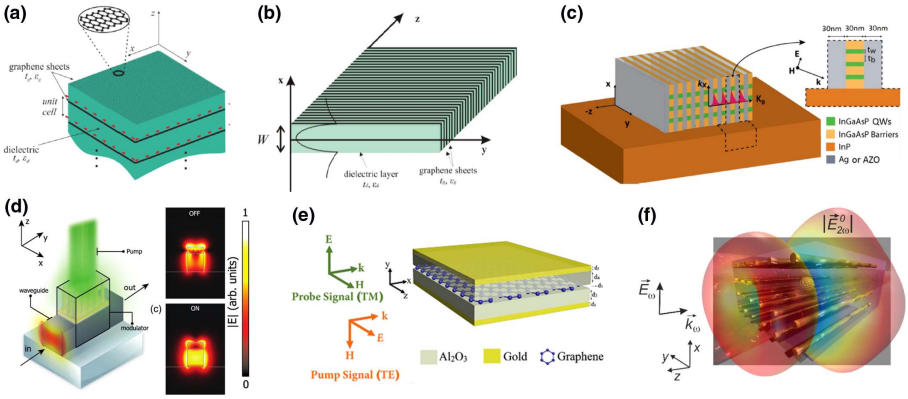

Active HMM for manipulating light propagation. (a), (b) Tuning of dispersion via chemical potential of graphene in multilayer HMM [26,126]. (c) Amplification of propagating waves via quantum well gain in lateral multilayer HMM [37]. (d) All-optical switch enabled by externally pumped nanowire HMM [11]. (e) Electro-optical and all-optical switch enabled by externally controlled graphene HMM [25,127]. (f) Second-harmonic generation of propagating light in nanowire HMM for high-sensitivity tomography [128]. (a) Reprinted with permission from [26]. Copyright 2016 Optical Society of America. (b) Reprinted with permission from [126]. Copyright 2017 Optical Society of America. (c) Reprinted with permission from [37]. Copyright 2015 Optical Society of America. (d) Reprinted with permission from [11]. Copyright 2014 Optical Society of America. (e) Reprinted with permission from [25]. Copyright 2015 Optical Society of America. (f) Reprinted with permission from [128]. Copyright 2015 Optical Society of America.

external bias for simultaneous phase (dispersion) and amplitude (gain/absorption) control of propagating waves. Further, the possibility for narrowband enhanced gain deserves to be scrutinized in greater detail, e.g., with self-consistent gain model beyond the effective medium theory.

Beyond graphene, electrides are 2D-like materials with electron transport naturally confined to a 2D plane. The electride Ca_2N was recently predicted to exhibit Type II hyperbolic dispersion over a broad wavelength range of 880–3300 nm [140]. The hyperbolic dispersion is predicted to have extremely low absorption loss and to be tunable via external strain.

5.2. Non-Reciprocal HMM

If both the time-reversal and inversion symmetry of an HMM is broken, then waves propagating through it exhibit non-reciprocity. That is, transmission from left to right does not equal transmission from right to left, which is the case for reciprocal systems.

5.2a. PT-Symmetric HMMs

Parity-time (PT) symmetric metamaterials are those in which the parity and time operators are simultaneously applicable, leading to non-Hermitian systems with purely real spectra [141]. PT symmetry is achieved in optical systems when the condition

$$n'(\mathbf{r}) + in''(\mathbf{r}) = n'(-\mathbf{r}) - in''(-\mathbf{r}) \tag{127}$$

is met for the spatially dependent complex refractive index. Therefore, achieving PT symmetry in optical systems necessarily requires active constituent materials. The enthusiasm surrounding PT-symmetric optical systems stems from their potential applications in such areas as one-way cloaking and super-focusing.

Wave propagation through PT-symmetric HMMs was analyzed theoretically in a one-dimensional multilayer with a unit cell consisting of a semiconductor HMM surrounded by dissipative and active semiconductor layers, with the imaginary permittivity of the dissipative and active layers being of equal magnitude but opposite sign [142]. Despite the entire system having a net zero imaginary permittivity, changes to the dispersion were observed upon tuning the imaginary permittivity of the passive and active layers from zero to non-zero values. Namely, transmission bands merge and exhibit a turning point with respect to the transverse wavenumber as the loss/gain in the system increases. Comparative calculations between the effective medium and exact multilayer illustrated that non-reciprocal behavior occurs for the latter. Namely, reflection spectra for left-to-right and right-to-left propagating waves had a slight difference in the exact case but not in the effective medium case, despite the operating wavelength being 100 times smaller than the multilayer lattice constant.

5.2b. Magneto-Optic HMM

A multilayer configuration consisting of a magneto-plasmonic material sandwiched between two different dielectric materials in the presence of an external magnetic field meets the criteria for non-reciprocity. Namely, the different dielectrics break the inversion symmetry while the magnetic field breaks time-reversal symmetry. This structure was analytically studied as a practical realization of a non-reciprocal HMM and was found to exhibit one-way topological transitions and non-reciprocal hyperbolic dispersion over a broad frequency range [143]. Namely, in the absence of a magnetic field, the transmission band of forward and backward high-k waves propagating along the crystal axis overlap spectrally. However, in the presence of a magnetic field normal to the crystal axis, the transmission band of the forward and backward waves blueshift and redshift, respectively. For a given wavelength, therefore, a significant extinction

ratio for forward and backward high-k transmission emerges with the applied magnetic field [143].

Formally, the electrical permittivity of the magneto-plasmonic constituent layer, $\widetilde{\epsilon_M}$, takes the form of a tensor with a unique diagonal component in the direction of the applied magnetic flux vector, **B**, and two degenerate diagonal components normal to **B**. The magnetic flux breaks the time-reversal symmetry in the direction normal to itself, along which there is also breaking of inversion symmetry. This is represented by two non-diagonal components of equal magnitude but opposite sign that couple the directions normal to **B**. Hence, assuming $\mathbf{B} = |\mathbf{B}|\mathbf{y}$ and taking the z-direction as the optical axis of the multilayer, the permittivity tensor for the magneto-plasmonic layer is written as

$$\widetilde{\epsilon_M} = \epsilon_0 \begin{bmatrix} \epsilon_{M,\perp B} & 0 & i\Delta_M \\ 0 & \epsilon_{M,\parallel B} & 0 \\ -i\Delta_M & 0 & \epsilon_{M,\perp B} \end{bmatrix}, \tag{128}$$

where

$$\epsilon_{M,\perp B} = \epsilon_\infty - \frac{\omega_p^2}{(\omega + i\gamma)^2 - \omega_B^2}\left(1 + \frac{\gamma}{\omega}\right), \tag{129}$$

$$\Delta_M = i\frac{\omega_B}{\omega}, \tag{130}$$

$$\epsilon_{M,\parallel B} = \epsilon_\infty - \frac{\omega_p^2}{\omega(\omega + i\gamma)}, \tag{131}$$

$$\omega_B = \frac{q}{m_{\text{eff}}}|\mathbf{B}|. \tag{132}$$

From this formalism, it is clear that observation of the effects of non-reciprocity are directly proportional to the magnetic field strength and sensitively depend on the losses in the system. Therefore, it is of great interest to reduce losses to observe the broadband non-reciprocity. This could be achieved by a well-designed HMM incorporating asymmetric gain layers around the magneto-plasmonic layer. In general, the problem of gain-enhanced non-reciprocal HMMs remains a fertile ground for exploration.

5.3. Long-Range Dipole Interactions

Thus far, we have described only the interaction between individual dipoles and HMMs, which lead to physical phenomena such as the Purcell factor, photonic spin Hall effect, super-Planckian heat transfer, and Cherenkov radiation. Additionally, intriguing physical phenomena may arise due to dipole–dipole interaction in the presence of HMMs. Namely, it was theoretically shown that both first-order effects, the cooperative lamb shift (CLS) and cooperative decay rate (CDR), and second-order effects, fluorescence resonant energy transfer (FRET) and the Casimir–Polder interaction potential (CPI), of dipole–dipole interactions may be significantly enhanced in the presence of HMMs [48]. Generally, the CLS and CDR are characterized by a modified emission wavelength and rate, respectively, occurring in an ensemble of N cold atoms that coherently interact through the absorption and re-emission of virtual photons [144].

In vacuum or conventional materials with elliptical dispersion, dipole–dipole interaction tends to weaken super-linearly with their separation distance. Hence the CLS and CDR are challenging to observe. However, it was shown that in the ideal lossless limit,

the effective interaction distance between two dipoles in a HMM can become vanishing small along the resonance cone angle specified by Eq. (123). This leads to giant enhancement of the CLS, CDR, FRET, and CPI. Further it was shown that interaction along the resonance cone reaches a maximum and minimum when the dipoles are both oriented normal and parallel to this angle, respectively, thus providing a degree-of-freedom for tuning the interaction strength. When realistic absorption losses were considered, significant enhancement of many-body phenomena remains a robust prediction. Several realistic platforms for experimentally studying the predicted enhanced dipole–dipole interaction were proposed, including multilayer Ag/TiO_2 at visible frequencies, multilayer hexagonal boron nitride in the mid-infrared, and a Ag/air visible frequency metasurface.

Figure 13 shows exemplary numerical results for two dipoles interacting with each other above a hyperbolic metasurface. A schematic of the interaction is shown in Fig. 13(a). The CLS normalized to the vacuum spontaneous emission rate is plotted in Fig. 13(b) as a function of relative angle between dipoles separated by 250 nm. A clear singularity in the CLS appears at the resonance cone angle in the HMM, in comparison to the CLS in vacuum and a lossy dielectric. The dependence of the normalized CLS on dipole–dipole separation distance along the resonance cone angle is shown in Fig. 13(c), wherein a significant enhancement of the CLS is observed to 400 nm. Enhancement in the FRET rate is shown in the inset of Fig. 13(c).

5.4. Electronic Addressability

We have presented different applications of HMMs based on different materials realizations, with great variety of geometries and designs. However, tunable HMMs are desired, at least for trimming its properties on specific applications, with the final objective of having total control of the device behavior. The integration of HMMs with electronic control then becomes one of the major challenges in the area.

The most conservative approach to the issue is leveraging the know-how of CMOS devices that commonly used contacts with pitches of just tens of nanometers. Metal-oxide-semiconductor technology has already been implemented on silicon photonics to locally modify the refractive index and material loss through the change of the depletion region, once an external electric field is applied [145]. The effect has also been used to allow ballistic transport on III-V nanowire junctions and change the carrier mobility on a InGaAs tri-gate nanowire field-effect transistor [146]. More recently, the depletion region control provided by the CMOS technology was applied to engineer the second-order optical non-linear susceptibility of an electronic metamaterial consisting of amorphous silicon and CMOS compatible metals, but still limited by the allowed number of periods [147]. There are still non-conservative approaches, like ionic conductance and conducting oxides. Ionic conductance was explored on random access memories with two electrodes sandwiching an ionic conductor between them. When a positive voltage is applied, a filament is created between the two electrodes resulting in a large change in the device resistance. A reverse bias dissolves the filament regenerating the original resistance. The effect was used by Thyagarajan *et al.* to control the reflection of two metasurfaces, consisting of nanostructured layers of Ag, alumina, and ITO, with ultralow voltage modulation [148]. Later, the use of conducting oxides, incorporated on a nanostructured layer, enabled the reflectance change due to field-effect modulation of the complex refractive index of the conductive oxide, also due to carrier depletion and accumulation control, provided by the CMOS technology [149]. Novel approaches should also be considered, for example, creating a HMM with a 2D phase-transition material or graphene, whose properties (e.g., absorption, polarizability, and dichroism) are temperature dependent and present a drastic variation due to a phase transition [137,150,151]. In these cases,

on-chip micro-coolers integrated with heaters could be used for local temperature control utilizing the Seebeck effect. The challenge imposed by electronic addressability has led to the development of new ideas and concepts, resulting in HMMs made of active III-V materials [57], phase-transition metamaterials [27], and tunable lenses [152], from which breakthrough devices will likely emerge.

5.5. Comparison to Other Systems

5.5a. All-Dielectric Metamaterials

After systematically reviewing the state-of-the-art of dynamically tunable and active HMMs, we have attained a vantage point from which we gaze the distant horizon. In the past several years, attention has shifted from plasmonic metamaterials, of which HMMs are a subset, toward all-dielectric metamaterials, with greater phase control and lower losses as prime motivating factors [153,154]. While plasmonic metamaterials inevitably suffer greater absorption losses than their dielectric counterparts, the higher optical density of states in plasmonic metamaterials make them the best candidate for applications requiring high-speed operation, super-resolution, and propagation over short distances in deeply subwavelength volumes [155].

5.5b. Single-Layer Plasmonics

In addition to the debate between plasmonic and dielectric metamaterials, arguments against HMMs in favor of single-layer plasmonic platforms have surfaced [115,156]. These arguments fail to recognize the inherently broadband response offered by HMMs, as well as the passively tunable response gained by using the ratio of the constituent materials as a design parameter.

We therefore anticipate continued efforts to optimize the material selection, device geometry, and fabrication processes to achieve HMM-based high-speed, high-efficiency sources with dynamic control of emission direction and polarization. Combining light-emitting and light-absorbing materials, such as compound semiconductors and TMD, intricately with hyperbolic metasurfaces and microfluidic components will open the door to compact optical systems [157,158], but still faces

Figure 13

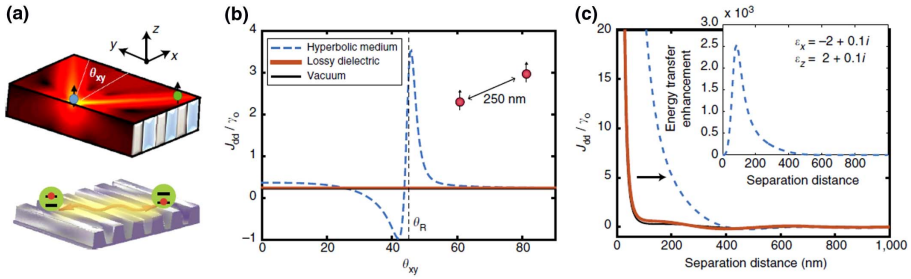

Enhanced dipole–dipole interactions in HMM [48]. (a) Schematic of two dipoles interacting with one another along the resonance cone angle above a hyperbolic metasurface. (b) Cooperative lamb shift normalized to the vacuum spontaneous emission rate, J_{dd}/γ_0, as a function of relative angle between dipoles separated for fixed separation distance of 250 nm. (c) Cooperative lamb shift normalized to the vacuum spontaneous emission rate, J_{dd}/γ_0, as a function of separation distance along the resonance cone angle. Inset of (c) shows rate enhancement of fluorescence energy transfer as a function of separation distance along the resonance cone angle. Reproduced from [48] under the terms of the Creative Commons Attribution 4.0 International License.

several technical challenges. Namely, processing of the active materials, for example by dry etching, often degrades their quality, leading to surface recombination and other forms of non-radiative losses. Strategies to clean and passivate materials during processing need to become more widely adopted, as has been recognized in the nano-laser community where the lasing threshold is understood to depend sensitively on processing conditions [159]. Additionally, the integration of HMMs with control electronics requires advanced design considerations and greater collaboration between experts in the optics community with those in the digital and RF electronics communities. For example, reconfigurable HMMs with local control of complex refractive index at the subwavelength scale could require electrodes separated by pitches of less than 100 nm. It would appear that this were most easily achieved if the skills and know-how of CMOS and silicon photonics engineers were leveraged by plasmonic device designers to co-design the optoelectronic response of active and tunable HMMs.

6. CONCLUSION

We have reviewed the state-of-the-art in dynamically tunable and active hyperbolic metamaterials. To fully appreciate the physical mechanisms responsible for tuning and optical gain, we first provided a comprehensive theoretical background, with the effective medium approximation appearing as the limiting case to the more general matrix methods and Bloch analysis. The major physics and applications of tunable and active HMMs were then presented, followed by emerging topics that point the way to new experimental ideas. We hope this review has been useful for the novice and expert alike. We look forward to witnessing the continued progress in bridging the intriguing physics offered by hyperbolic dispersion with the practical functionality offered by tunable and active constituent materials.

FUNDING

National Science Foundation (NSF) (1507146, EEC-0812072); Office of Naval Research (ONR) (N00014-13-1-0678).

ACKNOWLEDGMENT

The authors thank Dr. Conor T. Riley for contributing to the content of the section on thermophotovoltaics and Cheng-Yi Fang for conducting numerical simulations of the resonance cone angle.

REFERENCES

1. C. Cortes, W. Newman, S. Molesky, and Z. Jacob, "Quantum nanophotonics using hyperbolic metamaterials," J. Opt. **14**, 063001 (2012).
2. V. P. Drachev, V. A. Podolskiy, and A. V. Kildishev, "Hyperbolic metamaterials: new physics behind a classical problem," Opt. Express **21**, 15048–15064 (2013).
3. A. Poddubny, I. Iorsh, P. Belov, and Y. Kivshar, "Hyperbolic metamaterials," Nat. Photonics **7**, 948–957 (2013).
4. P. Shekhar, J. Atkinson, and Z. Jacob, "Hyperbolic metamaterials: fundamentals and applications," Nano Converg. **1**, 14–17 (2014).
5. L. Ferrari, C. Wu, D. Lepage, X. Zhang, and Z. Liu, "Hyperbolic metamaterials and their applications," Prog. Quantum Electron. **40**, 1–40 (2015).
6. Z. Liu, H. Lee, Y. Xiong, C. Sun, and X. Zhang, "Far-field optical hyperlens magnifying sub-diffraction-limited objects," Science **315**, 1686 (2007).
7. H. Lee, Z. Liu, Y. Xiong, C. Sun, and X. Zhang, "Development of optical hyperlens for imaging below the diffraction limit," Opt. Express **15**, 15886–15891 (2007).

8. H. N. S. Krishnamoorthy, Z. Jacob, E. Narimanov, and V. M. Menon, "Topological transitions in metamaterials," Science **336**, 205–209 (2012).
9. D. Lu, J. Kan, E. Fullerton, and Z. Liu, "Enhancing spontaneous emission rates of molecules using nanopatterned multilayer hyperbolic metamaterials," Nat. Nanotechnol. **9**, 48–53 (2014).
10. A. V. Zayats, "Nonlinear hyperbolic metamaterials," in *8th International Congress on Advanced Electromagnetic Materials in Microwaves and Optics* (IEEE, 2014), pp. 431–432.
11. A. D. Neira, G. A. Wurtz, P. Ginzburg, and A. V. Zayats, "Ultrafast all-optical modulation with hyperbolic metamaterial integrated in Si photonic circuitry," Opt. Express **22**, 10987–10994 (2014).
12. X. Ao and C. T. Chan, "Far-field image magnification for acoustic waves using anisotropic acoustic metamaterials," Phys. Rev. E **77**, 025601 (2008).
13. C. Shen, Y. Xie, N. Sui, W. Wang, S. A. Cummer, and Y. Jing, "Broadband acoustic hyperbolic metamaterial," Phys. Rev. Lett. **115**, 254301 (2015).
14. D. R. Smith and D. Schurig, "Electromagnetic wave propagation in media with indefinite permittivity and permeability tensors," Phys. Rev. Lett. **90**, 077405 (2003).
15. E. E. Narimanov and A. V. Kildishev, "Metamaterials: naturally hyperbolic," Nat. Photonics **9**, 214–216 (2015).
16. A. J. Hoffman, L. Alekseyev, S. S. Howard, K. J. Franz, D. Wasserman, V. A. Podolskiy, E. E. Narimanov, D. L. Sivco, and C. Gmachl, "Negative refraction in semiconductor metamaterials," Nat. Mater. **6**, 946–950 (2007).
17. P. Shekhar and Z. Jacob, "Strong coupling in hyperbolic metamaterials," Phys. Rev. B **90**, 045313 (2014).
18. S. Maier, *Plasmonics: Fundamentals and Applications* (Springer, 2007).
19. K. M. McPeak, S. V. Jayanti, S. J. P. Kress, S. Meyer, S. Iotti, A. Rossinelli, and D. J. Norris, "Plasmonic films can easily be better: rules and recipes," ACS Photon. **2**, 326–333 (2015).
20. G. Naik, J. Liu, A. Kildishev, V. Shalaev, and A. Boltasseva, "Demonstration of Al:ZnO as a plasmonic component for near-infrared metamaterials," Proc. Natl. Acad. Sci. U. S. A. **109**, 8834–8838 (2011).
21. C. T. Riley, T. A. Kieu, J. S. T. Smalley, S. H. A. Pan, S. J. Kim, K. W. Post, A. Kargar, D. N. Basov, X. Pan, Y. Fainman, D. Wang, and D. J. Sirbuly, "Plasmonic tuning of aluminum doped zinc oxide nanostructures by atomic layer deposition," Physica Status Solidi **8**, 948–952 (2014).
22. C. T. Riley, J. S. T. Smalley, K. W. Post, D. N. Basov, Y. Fainman, D. Wang, Z. Liu, and D. J. Sirbuly, "High-quality, ultraconformal aluminum-doped zinc oxide nanoplasmonic and hyperbolic metamaterials," Small **12**, 892–901 (2016).
23. C. Z. Ning and J. V. Moloney, "Thermal effects on the threshold of vertical-cavity surface-emitting lasers: first- and second-order phase transitions," Opt. Lett. **20**, 1151–1153 (1995).
24. W.-C. Ng, Y. Liu, and K. Hess, "Lattice temperature model and temperature effects in oxide-confined VCSEL's," J. Comput. Electron. **3**, 103–116 (2004).
25. M. Shoaei, M. K. Moravvej-Farshi, and L. Yousefi, "All-optical switching of nonlinear hyperbolic metamaterials in visible and near-infrared regions," J. Opt. Soc. Am. B **32**, 2358–2365 (2015).
26. B. Janaszek, A. Tyszka-Zawadzka, and P. Szczepański, "Tunable graphene-based hyperbolic metamaterial operating in SCLU telecom bands," Opt. Express **24**, 24129–24136 (2016).
27. H. N. S. Krishnamoorthy, Y. Zhou, S. Ramanathan, E. Narimanov, and V. M. Menon, "Tunable hyperbolic metamaterials utilizing phase change heterostructures," Appl. Phys. Lett. **104**, 121101 (2014).

28. S. Prayakarao, B. Mendoza, A. Devine, C. Kyaw, R. B. van Dover, V. Liberman, and M. A. Noginov, "Tunable VO_2/Au hyperbolic metamaterial," Appl. Phys. Lett. **109**, 061105 (2016).
29. A. Fang, T. Koschny, M. Wegener, and C. M. Soukoulis, "Self-consistent calculation of metamaterials with gain," Phys. Rev. B **79**, 241104 (2009).
30. A. Fang, T. Koschny, and C. Soukoulis, "Lasing in metamaterial nanostructures," J. Opt. **12**, 024013 (2010).
31. S. Wuestner, A. Pusch, K. Tsakmakidis, J. Hamm, and O. Hess, "Gain and plasmon dynamics in active negative-index metamaterials," Philos. Trans. R. Soc. London, Ser. A **369**, 3525–3550 (2011).
32. Y. T. Wang, B. H. Cheng, Y. Z. Ho, Y.-C. Lan, P.-G. Luan, and D. P. Tsai, "Gain-assisted hybrid-superlens hyperlens for nano imaging," Opt. Express **20**, 22953–22960 (2012).
33. T. Aisaka, M. Fujii, and S. Hayashi, "Enhancement of upconversion luminescence of Er doped Al_2O_3 films by Ag island films," Appl. Phys. Lett. **92**, 132105 (2008).
34. E. Desurvire, *Erbium-Doped Fiber Amplifiers* (Wiley, 1994).
35. K. Ravi, Q. Wang, and S.-T. Ho, "A multi-band, multi-level, multi-electron model for efficient FDTD simulations of electromagnetic interactions with semiconductor quantum wells," J. Mod. Opt. **62**, 1158–1182 (2015).
36. J. Smalley, F. Vallini, B. Kante, and Y. Fainman, "Modal amplification in active waveguides with hyperbolic dispersion at telecommunication frequencies," Opt. Express **22**, 21088–21105 (2014).
37. J. Smalley, F. Vallini, S. Shahin, B. Kante, and Y. Fainman, "Gain-enhanced high-k transmission through metal-semiconductor hyperbolic metamaterials," Opt. Mater. Express **5**, 2300–2312 (2015).
38. L. Coldren, S. Corzine, and M. Masanovic, "Gain and current relations," in *Diode Lasers and Photonic Integrated Circuits* (Wiley, 2012), pp. 157–246.
39. J. Smalley, Q. Gu, and Y. Fainman, "Temperature dependence of the spontaneous emission factor in subwavelength semiconductor lasers," IEEE J. Quantum Electron. **50**, 175–185 (2014).
40. G. Agrawal and N. Dutta, *Semiconductor Lasers*, 2nd ed. (Van Nostrand Reinhold, 1993).
41. P. Berini, "Long-range surface plasmon polaritons," Adv. Opt. Photonics **1**, 484–588 (2009).
42. E. Economou, "Surface plasmons in thin films," Phys. Rev. **182**, 539–554 (1969).
43. I. Avrutsky, I. Salakhutdinov, J. Elser, and V. Podolskiy, "Highly confined optical modes in nanoscale metal-dielectric multilayers," Phys. Rev. B **75**, 241402 (2007).
44. J. Schilling, "Uniaxial metallo-dielectric metamaterials with scalar positive permeability," Phys. Rev. E **74**, 046618 (2006).
45. J. D. Caldwell, A. V. Kretinin, Y. Chen, V. Giannini, M. M. Fogler, Y. Francescato, C. T. Ellis, J. G. Tischler, C. R. Woods, A. J. Giles, M. Hong, K. Watanabe, T. Taniguchi, S. A. Maier, and K. S. Novoselov, "Sub-diffractional volume-confined polaritons in the natural hyperbolic material hexagonal boron nitride," Nat. Commun. **5**, 5221 (2014).
46. S. Dai, Z. Fei, Q. Ma, A. S. Rodin, M. Wagner, A. S. McLeod, M. K. Liu, W. Gannett, W. Regan, K. Watanabe, T. Taniguchi, M. Thiemens, G. Dominguez, A. H. C. Neto, A. Zettl, F. Keilmann, P. Jarillo-Herrero, M. M. Fogler, and D. N. Basov, "Tunable phonon polaritons in atomically thin van der Waals crystals of boron nitride," Science **343**, 1125–1129 (2014).

47. P. Li, X. Yang, T. W. W. Maß, J. Hanss, M. Lewin, A.-K. U. Michel, M. Wuttig, and T. Taubner, "Reversible optical switching of highly confined phonon-polaritons with an ultrathin phase-change material," Nat. Mater. **15**, 870–875 (2016).
48. C. L. Cortes and Z. Jacob, "Super-Coulombic atom-atom interactions in hyperbolic media," Nat. Commun. **8**, 14144 (2017).
49. E. M. Purcell, H. C. Torrey, and R. V. Pound, "Resonance absorption by nuclear magnetic moments in a solid," Phys. Rev. **69**, 37–38 (1946).
50. W. L. Barnes, "Fluorescence near interfaces: the role of photonic mode density," J. Mod. Opt. **45**, 661–699 (1998).
51. P. Johnson and R. Christy, "Optical constants of noble metals," Phys. Rev. B **6**, 4370–4379 (1972).
52. A. Yariv and P. Yeh, "Optical resonators," in *Photonics: Optical Electronics in Modern Communication Systems* (Oxford, 2007), p. 156.
53. D. Ko and J. Sambles, "Scattering matrix method for propagation of radiation in stratified media: attenuated total reflection studies of liquid crystals," J. Opt. Soc. Am. A **5**, 1863–1866 (1988).
54. D. Ko and J. Inkson, "Matrix method for tunneling in heterostructures: resonant tunneling in multilayer systems," Phys. Rev. B **38**, 9945–9951 (1988).
55. F. Krayzel, R. Polles, A. Moreau, M. Mihailovic, and G. Granet, "Simulation and analysis of exotic non-specular phenomena," J. Eur. Opt. Soc. **5**, 10025 (2010).
56. S. Chang and A. Taflove, "Finite-difference time-domain model of lasing action in a four-level two-electron atomic system," Opt. Express **12**, 3827–3843 (2004).
57. J. S. T. Smalley, F. Vallini, S. A. Montoya, L. Ferrari, S. Shahin, C. T. Riley, B. Kanté, E. E. Fullerton, Z. Liu, and Y. Fainman, "Luminescent hyperbolic metasurfaces," Nat. Commun. **8**, 13793 (2017).
58. A. Yariv and P. Yeh, "Wave propagation in periodic media," in *Photonics: Optical Electronics in Modern Communications* (Oxford University, 2007), pp. 539–601.
59. A. Orlov, I. Iorsh, P. Belov, and Y. Kivshar, "Complex band structure of nanostructured metal-dielectric metamaterials," Opt. Express **21**, 1593–1598 (2013).
60. S. Rytov, "Electromagnetic properties of a finely stratified medium," J. Exp. Theor. Phys. **2**, 466–475 (1956).
61. V. Podolskiy, "Anisotropic and hyperbolic metamaterials," in *Tutorials in Metamaterials*, M. Noginov and V. Podolskiy, eds. (CRC Press, 2012), pp. 163–207.
62. S. S. Kruk, Z. J. Wong, E. Pshenay-Severin, K. O'Brien, D. N. Neshev, Y. S. Kivshar, and X. Zhang, "Magnetic hyperbolic optical metamaterials," Nat. Commun. **7**, 11329 (2016).
63. F. Xu, C.-C. Cheng, A. Scherer, R.-C. Tyan, P.-C. Sun, and Y. Fainman, "Form-birefringent computer-generated holograms," Opt. Lett. **21**, 1513–1515 (1996).
64. F. V. Bunkin, "On radiation in anisotropic media," Sov. Phys. JETP **5**, 277–283 (1957).
65. H. H. Kuehl, "Electromagnetic radiation from an electric dipole in a cold anisotropic plasma," Phys. Fluids **5**, 1095–1103 (1962).
66. H. Staras, "The 'infinity catastrophe' associated with radiation in magnetoionic media," Radio Sci. **1**, 1013–1020 (1966).
67. R. K. Fisher and R. W. Gould, "Resonance cones in the field pattern of a short antenna in an anisotropic plasma," Phys. Rev. Lett. **22**, 1093–1095 (1969).
68. K. Balmain, A. Luttgen, and P. Kremer, "Resonance cone formation, reflection, refraction, and focusing in a planar anisotropic metamaterial," IEEE Antennas Wireless Propag. Lett. **1**, 146–149 (2002).

69. K. Balmain, A. Luttgen, and P. Kremer, "Power flow for resonance cone phenomena in planar anisotropic metamaterials," IEEE Trans. Antennas Propag. **51**, 2612–2618 (2003).
70. D. de Ceglia, M. A. Vincenti, S. Campione, F. Capolino, J. W. Haus, and M. Scalora, "Second-harmonic double-resonance cones in dispersive hyperbolic metamaterials," Phys. Rev. B **89**, 075123 (2014).
71. L. Gu, T. U. Tumkur, G. Zhu, and M. A. Noginov, "Blue shift of spontaneous emission in hyperbolic metamaterial," Sci. Rep. **4**, 4969 (2014).
72. M. Y. Shalaginov, V. V. Vorobyov, J. Liu, M. Ferrera, A. V. Akimov, A. Lagutchev, A. N. Smolyaninov, V. V. Klimov, J. Irudayaraj, A. V. Kildishev, A. Boltasseva, and V. M. Shalaev, "Enhancement of single-photon emission from nitrogen-vacancy centers with TiN/(Al, Sc)N hyperbolic metamaterial," Laser Photonics Rev. **9**, 120–127 (2015).
73. K. V. Sreekanth, T. Biaglow, and G. Strangi, "Directional spontaneous emission enhancement in hyperbolic metamaterials," J. Appl. Phys. **114**, 134306 (2013).
74. T. Galfsky, H. Krishnamoorthy, W. Newman, E. Narimanov, Z. Jacob, and V. Menon, "Active hyperbolic metamaterials: enhanced spontaneous emission and light extraction," Optica **2**, 62–65 (2015).
75. L. Ferrari, J. S. T. Smalley, Y. Fainman, and Z. Liu, "Hyperbolic metamaterials for dispersion-assisted directional light emission," Nanoscale **9**, 9034–9048 (2017).
76. P. N. Dyachenko, S. Molesky, A. Y. Petrov, M. Stormer, T. Krekeler, S. Lang, M. Ritter, Z. Jacob, and M. Eich, "Controlling thermal emission with refractory epsilon-near-zero metamaterials via topological transitions," Nat. Commun. **7**, 11809 (2016).
77. A. V. Shchegrov, K. Joulain, R. Carminati, and J.-J. Greffet, "Near-field spectral effects due to electromagnetic surface excitations," Phys. Rev. Lett. **85**, 1548–1551 (2000).
78. M. Florescu, K. Busch, and J. P. Dowling, "Thermal radiation in photonic crystals," Phys. Rev. B **75**, 201101 (2007).
79. E. E. Narimanov and I. I. Smolyaninov, "Beyond Stefan-Boltzmann law: thermal hyper-conductivity," arXiv: 1109.5444 (2011).
80. Y. Guo and Z. Jacob, "Thermal hyperbolic metamaterials," Opt. Express **21**, 15014–15019 (2013).
81. X. Liu and Z. Zhang, "Near-field thermal radiation between metasurfaces," ACS Photonics **2**, 1320–1326 (2015).
82. J. Dai, F. Ding, S. I. Bozhevolnyi, and M. Yan, "Ultrabroadband super-Planckian radiative heat transfer with artificial continuum cavity states in patterned hyperbolic metamaterials," Phys. Rev. B **95**, 245405 (2017).
83. I. S. Nefedov and L. A. Melnikov, "Super-Planckian far-zone thermal emission from asymmetric hyperbolic metamaterials," Appl. Phys. Lett. **105**, 161902 (2014).
84. S. I. Maslovski, C. R. Simovski, and S. A. Tretyakov, "Overcoming black body radiation limit in free space: metamaterial superemitter," New J. Phys. **18**, 013034 (2016).
85. K. Sreekanth, K. Krishna, A. De Luca, and G. Strangi, "Large spontaneous emission rate enhancement in grating coupled hyperbolic metamaterials," Sci. Rep. **4**, 6340 (2014).
86. K. Sreekanth, A. De Luca, and G. Strangi, "Excitation of volume plasmon polaritons in metal-dielectric metamaterials using 1D and 2D diffraction gratings," J. Opt. **16**, 105103 (2014).
87. E. E. Narimanov, "Photonic hypercrystals," Phys. Rev. X **4**, 041014 (2014).

88. T. Galfsky, J. Gu, E. E. Narimanov, and V. M. Menon, "Photonic hypercrystals for control of light-matter interactions," Proc. Natl. Acad. Sci. U. S. A. **114**, 5125–5129 (2017).
89. T. Galfsky, Z. Sun, C. R. Considine, C.-T. Chou, W.-C. Ko, Y.-H. Lee, E. E. Narimanov, and V. M. Menon, "Broadband enhancement of spontaneous emission in two-dimensional semiconductors using photonic hypercrystals," Nano Lett. **16**, 4940–4945 (2016).
90. A. High, R. Devlin, A. Dibos, M. Polking, D. Wild, J. Perczel, N. de Leon, M. Lukin, and H. Park, "Visible-frequency hyperbolic metasurface," Nature **522**, 192–196 (2015).
91. F. Liu, L. Xiao, M. Wang, K. Cui, X. Feng, W. Zhang, and Y. Huang, "Integrated Cherenkov radiation emitter eliminating the electron velocity threshold," Nat. Photonics **11**, 289–292 (2017).
92. Z. Jacob, L. Alekseyev, and E. Narimanov, "Optical hyperlens: far-field imaging beyond the diffraction limit," Opt. Express **14**, 8247–8256 (2006).
93. J. Rho, Z. Ye, Y. Xiong, Z. Liu, H. Choi, G. Bartal, and X. Zhang, "Spherical hyperlens for two-dimensional sub-diffractional imaging at visible frequencies," Nat. Commun. **1**, 143 (2010).
94. J. Sun, M. Shalaev, and N. Litchinitser, "Experimental demonstration of a non-resonant hyperlens in the visible spectral range," Nat. Commun. **6**, 7201 (2015).
95. M. Byun, D. Lee, M. Kim, Y. Kim, K. Kim, J. Ok, J. Rho, and H. Lee, "Demonstration of nanoimprinted hyperlens array for high-throughput sub-diffraction imaging," Sci. Rep. **7**, 46314 (2017).
96. X. Yin, Z. Ye, J. Rho, Y. Wang, and X. Zhang, "Photonic spin Hall effect at metasurfaces," Science **339**, 1405–1407 (2013).
97. P. Kapitanova, P. Ginzburg, F. Rodriguez-Fortuno, D. Filonov, P. Voroshilov, P. Belov, A. Poddubny, Y. Kivshar, A. Wurtz, and A. Zayats, "Photonic spin Hall effect in hyperbolic metamaterials for polarization-controlled routing of sub-wavelength modes," Nat. Commun. **5**, 3226 (2014).
98. J. Petersen, J. Volz, and A. Rauschenbeutel, "Chiral nanophotonic waveguide interface based on spin-orbit interaction of light," Science **346**, 67–71 (2014).
99. P. A. Cherenkov, "Visible emission of clean liquids by action of gamma radiation," Dokl. Akad. Nauk SSSR **2**, 451–454 (1934).
100. P. Genevet, D. Wintz, A. Ambrosio, A. She, R. Blanchard, and F. Capasso, "Controlled steering of Cherenkov surface plasmon wakes with a one-dimensional metamaterial," Nat. Nanotechnol. **10**, 804–809 (2015).
101. V. Veselago, "The electrodynamics of substances with simultaneously negative values of epsilon and mu," Sov. Phys. Usp. **10**, 509–514 (1968).
102. A. Grbic and G. V. Eleftheriades, "Experimental verification of backward-wave radiation from a negative refractive index metamaterial," J. Appl. Phys. **92**, 5930–5935 (2002).
103. S. Xi, H. Chen, T. Jiang, L. Ran, J. Huangfu, B.-I. Wu, J. A. Kong, and M. Chen, "Experimental verification of reversed Cherenkov radiation in left-handed metamaterial," Phys. Rev. Lett. **103**, 194801 (2009).
104. Z. Duan, X. Tang, Z. Wang, Y. Zhang, X. Chen, M. Chen, and Y. Gong, "Observation of the reversed Cherenkov radiation," Nat. Commun. **8**, 14901 (2017).
105. A. M. Shaltout, N. Kinsey, J. Kim, R. Chandrasekar, J. C. Ndukaife, A. Boltasseva, and V. M. Shalaev, "Development of optical metasurfaces: emerging concepts and new materials," Proc. IEEE **104**, 2270–2287 (2016).
106. C. Argyropoulos, N. Estakhri, F. Monticone, and A. Alu, "Negative refraction, gain, and nonlinear effects in hyperbolic metamaterials," Opt. Express **21**, 15037–15047 (2013).

107. C. Duncan, L. Perret, S. Palomba, M. Lapine, B. Kuhlmey, and C. de Sterke, "New avenues for phase matching in nonlinear hyperbolic metamaterials," Sci. Rep. **5**, 8983 (2015).
108. Y. J. Ding and J. B. Khurgin, "Second-harmonic generation based on quasi-phase matching: a novel configuration," Opt. Lett. **21**, 1445–1447 (1996).
109. A. N. Poddubny, I. V. Iorsh, and A. A. Sukhorukov, "Generation of photon-plasmon quantum states in nonlinear hyperbolic metamaterials," Phys. Rev. Lett. **117**, 123901 (2016).
110. J. J. D. McKendry, R. P. Green, A. E. Kelly, Z. Gong, B. Guilhabert, D. Massoubre, E. Gu, and M. D. Dawson, "High-speed visible light communications using individual pixels in a micro light-emitting diode array," IEEE Photonics Technol. Lett. **22**, 1346–1348 (2010).
111. L. J. Wong, I. Kaminer, O. Ilic, J. D. Joannopoulos, and M. Soljačić, "Towards graphene plasmon-based free-electron infrared to X-ray sources," Nat. Photonics **10**, 46–52 (2015).
112. X. Ni, S. Ishii, M. Thoreson, V. Shalaev, S. Han, S. Lee, and A. Kildishev, "Loss-compensated and active hyperbolic metamaterials," Opt. Express **19**, 25242–25254 (2011).
113. R. Savelev, I. Shadrivov, P. Belov, N. Rosanov, S. Fedorov, A. Sukhorukov, and Y. Kivshar, "Loss compensation in metal-dielectric layered metamaterials," Phys. Rev. B **87**, 115139 (2013).
114. R. Savelev, I. Shadrivov, and Y. Kivshar, "Wave scattering by metal-dielectric multilayer structures with gain," JETP Lett. **100**, 731–736 (2014).
115. T. Li, V. Nagal, D. H. Gracias, and J. B. Khurgin, "Limits of imaging with multilayer hyperbolic metamaterials," Opt. Express **25**, 13588–13601 (2017).
116. E. E. Narimanov, "Hyperstructured illumination," ACS Photonics **3**, 1090–1094 (2016).
117. M. G. Gustafsson, "Surpassing the lateral resolution limit by a factor of two using structured illumination microscopy," J. Microsc. **198**, 82–87 (2000).
118. E. Khan and E. E. Narimanov, "Hyperstructured illumination in disordered media," Appl. Phys. Lett. **111**, 051105 (2017).
119. Q. Ma, H. Hu, E. Huang, and Z. Liu, "Super-resolution imaging by metamaterial-based compressive spatial-to-spectral transformation," Nanoscale **9**, 18268–18274 (2017).
120. G. T. Dempsey, J. C. Vaughan, K. H. Chen, M. Bates, and X. Zhuang, "Evaluation of fluorophores for optimal performance in localization-based super-resolution imaging," Nat. Methods **8**, 1027–1036 (2011).
121. S. Ishii, M. Y. Shalaginov, V. E. Babicheva, A. Boltasseva, and A. V. Kildishev, "Plasmonic waveguides cladded by hyperbolic metamaterials," Opt. Lett. **39**, 4663–4666 (2014).
122. V. E. Babicheva, M. Y. Shalaginov, S. Ishii, A. Boltasseva, and A. V. Kildishev, "Long-range plasmonic waveguides with hyperbolic cladding," Opt. Express **23**, 31109–31119 (2015).
123. V. E. Babicheva, M. Y. Shalaginov, S. Ishii, A. Boltasseva, and A. V. Kildishev, "Finite-width plasmonic waveguides with hyperbolic multilayer cladding," Opt. Express **23**, 9681–9689 (2015).
124. Y. Tang, Z. Xi, M. Xu, S. Bäumer, A. J. L. Adam, and H. P. Urbach, "Spatial mode-selective waveguide with hyperbolic cladding," Opt. Lett. **41**, 4285–4288 (2016).
125. T. Xu and H. Lezec, "Visible-frequency asymmetric transmission devices incorporating a hyperbolic metamaterial," Nat. Commun. **5**, 4141 (2014).
126. A. Tyszka-Zawadzka, B. Janaszek, and P. Szczepański, "Tunable slow light in graphene-based hyperbolic metamaterial waveguide operating in SCLU telecom bands," Opt. Express **25**, 7263–7272 (2017).

127. M. Shoaei, M. K. Moravvej-Farshi, and L. Yousefi, "Nanostructured graphene-based hyperbolic metamaterial performing as a wide-angle near infrared electro-optical switch," Appl. Opt. **54**, 1206–1211 (2015).
128. P. Segovia, G. Marino, A. V. Krasavin, N. Olivier, G. A. Wurtz, P. A. Belov, P. Ginzburg, and A. V. Zayats, "Hyperbolic metamaterial antenna for second-harmonic generation tomography," Opt. Express **23**, 30730–30738 (2015).
129. W. Shockley and H. J. Queisser, "Detailed balance limit of efficiency of p-n junction solar cells," J. Appl. Phys. **32**, 510–519 (1961).
130. T. Coutts, "A review of progress in thermophotovoltaic generation of electricity," Renew. Sustain. Energy Rev. **3**, 77–184 (1999).
131. A. Lenert, D. M. Bierman, Y. Nam, W. R. Chan, I. Celanović, M. Soljačić, and E. N. Wang, "A nanophotonic solar thermophotovoltaic device," Nat. Nanotechnol. **9**, 126–130 (2014).
132. C. Riley, T. Kieu, J. Smalley, S. Pan, S. Kim, K. Post, A. Kargar, D. Basov, X. Pan, Y. Fainman, D. Wang, and D. Sirbuly, "Plasmonic tuning of aluminum doped zinc oxide nanostructures by atomic layer deposition," Phys. Status Solidi (RRL) **8**, 948–952 (2014).
133. C. T. Riley, J. S. T. Smalley, J. R. J. Brodie, Y. Fainman, D. J. Sirbuly, and Z. Liu, "Near-perfect broadband absorption from hyperbolic metamaterial nanoparticles," Proc. Natl. Acad. Sci. U. S. A. **114**, 1264–1268 (2017).
134. S. Molesky, C. J. Dewalt, and Z. Jacob, "High temperature epsilon-near-zero and epsilon-near-pole metamaterial emitters for thermophotovoltaics," Opt. Express **21**, A96–A110 (2013).
135. Y.-C. Chang, C.-H. Liu, C.-H. Liu, S. Zhang, S. R. Marder, E. E. Narimanov, Z. Zhong, and T. B. Norris, "Realization of mid-infrared graphene hyperbolic metamaterials," Nat. Commun. **7**, 10568 (2016).
136. J. S. Gomez-Diaz, M. Tymchenko, and A. Alù, "Hyperbolic metasurfaces: surface plasmons, light-matter interactions, and physical implementation using graphene strips [Invited]," Opt. Mater. Express **5**, 2313–2329 (2015).
137. S. Dai, Q. Ma, M. K. Liu, T. Andersen, Z. Fei, M. D. Goldflam, M. Wagner, K. Watanabe, T. Taniguchi, M. Thiemens, F. Keilmann, G. C. A. M. Janssen, S.-E. Zhu, P. Jarillo-Herrero, M. M. Fogler, and D. N. Basov, "Graphene on hexagonal boron nitride as a tunable hyperbolic metamaterial," Nat. Nanotechnol. **10**, 682–686 (2015).
138. S. Dai, Q. Ma, T. Andersen, A. S. Mcleod, Z. Fei, M. K. Liu, M. Wagner, K. Watanabe, T. Taniguchi, M. Thiemens, F. Keilmann, P. Jarillo-Herrero, M. M. Fogler, and D. N. Basov, "Subdiffractional focusing and guiding of polaritonic rays in a natural hyperbolic material," Nat. Commun. **6**, 6963 (2015).
139. B. Janaszek, A. Tyszka-Zawadzka, and P. Szczepański, "Control of gain/absorption in tunable hyperbolic metamaterials," Opt. Express **25**, 13153–13162 (2017).
140. S. Guan, S. Y. Huang, Y. Yao, and S. A. Yang, "Tunable hyperbolic dispersion and negative refraction in natural electride materials," Phys. Rev. B **95**, 165436 (2017).
141. C. M. Bender and S. Boettcher, "Real spectra in non-Hermitian Hamiltonians having PT symmetry," Phys. Rev. Lett. **80**, 5243–5246 (1998).
142. O. V. Shramkova and G. P. Tsironis, "Propagation of electromagnetic waves in PT-symmetric hyperbolic structures," Phys. Rev. B **94**, 035141 (2016).
143. A. Leviyev, B. Stein, A. Christofi, T. Galfsky, H. Krishnamoorthy, I. L. Kuskovsky, V. Menon, and A. B. Khanikaev, "Nonreciprocity and one-way topological transitions in hyperbolic metamaterials," APL Photonics **2**, 076103 (2017).
144. J. Manassah, "Cooperative radiation from atoms in different geometries: decay rate and frequency shift," Adv. Opt. Photonics **4**, 108–156 (2012).

145. R. Sharma, M. W. Puckett, H.-H. Lin, A. Isichenko, F. Vallini, and Y. Fainman, "Effect of dielectric claddings on the electro-optic behavior of silicon waveguides," Opt. Lett. **41**, 1185–1188 (2016).
146. A. V. Thathachary, N. Agrawal, L. Liu, and S. Datta, "Electron transport in multi-gate $In_xGa_{1-x}As$ nanowire FETs: from diffusive to ballistic regimes at room temperature," Nano Lett. **14**, 626–633 (2014).
147. H.-H. Lin, F. Vallini, M.-H. Yang, R. Sharma, M. W. Puckett, S. Montoya, C. D. Wurm, E. E. Fullerton, and Y. Fainman, "Electronic metamaterials with tunable second-order optical nonlinearities," Sci. Rep. **7**, 9983 (2017).
148. K. Thyagarajan, R. Sokhoyan, L. Zornberg, and H. A. Atwater, "Millivolt modulation of plasmonic metasurface optical response via ionic conductance," Adv. Mater. **29**, 1701044 (2017).
149. Y.-W. Huang, H. W. H. Lee, R. Sokhoyan, R. A. Pala, K. Thyagarajan, S. Han, D. P. Tsai, and H. A. Atwater, "Gate-tunable conducting oxide metasurfaces," Nano Lett. **16**, 5319–5325 (2016).
150. J. Rensberg, S. Zhang, Y. Zhou, A. S. McLeod, C. Schwarz, M. Goldflam, M. Liu, J. Kerbusch, R. Nawrodt, S. Ramanathan, D. N. Basov, F. Capasso, C. Ronning, and M. A. Kats, "Active optical metasurfaces based on defect-engineered phase-transition materials," Nano Lett. **16**, 1050–1055 (2016).
151. M. A. K. Othman, C. Guclu, and F. Capolino, "Graphene-based tunable hyperbolic metamaterials and enhanced near-field absorption," Opt. Express **21**, 7614–7632 (2013).
152. A. She, S. Zhang, S. Shian, D. Clarke, and F. Capasso, "Large area electrically tunable metasurface lenses," in *Conference on Lasers and Electro-Optics* (OSA, 2017), paper FTu3G.4.
153. S. Jahani and Z. Jacob, "All-dielectric metamaterials," Nat. Nanotechnol. **11**, 23–36 (2016).
154. P. Genevet, F. Capasso, F. Aieta, M. Khorasaninejad, and R. Devlin, "Recent advances in planar optics: from plasmonic to dielectric metasurfaces," Optica **4**, 139–152 (2017).
155. K. Liu, S. Sun, A. Majumdar, and V. Sorger, "Fundamental scaling laws in nanophotonics," Sci. Rep. **6**, 37419 (2016).
156. T. Li and J. Khurgin, "Hyperbolic metamaterials: beyond the effective medium theory," Optica **3**, 1388–1396 (2016).
157. K. V. Sreekanth, Y. Alapan, M. ElKabbash, E. Ilker, M. Hinczewski, U. A. Gurkan, A. De Luca, and G. Strangi, "Extreme sensitivity biosensing platform based on hyperbolic metamaterials," Nat. Mater. **15**, 621–627 (2016).
158. J. Smalley, F. Vallini, and Y. Fainman, "Detection of optical activity with diode-integrated hyperbolic metasurfaces," Biomed. Opt. Express **8**, 5594–5603 (2017).
159. A. Higuera-Rodriguez, B. Romeira, S. Birindelli, L. E. Black, E. Smalbrugge, P. J. van Veldhoven, W. M. Kessels, M. K. Smit, and A. Fiore, "Ultra-low surface recombination velocity in passivated InGaAs/InP nanopillars," Nano Lett. **17**, 2627–2633 (2017).

Joseph S. T. Smalley received the B.S. (2011) degree in engineering science from Penn State University and the M.S. (2013) and Ph.D. (2016) degrees in electrical engineering from the University of California, San Diego. Under the supervision of Prof. Shaya Fainman, his Ph.D. research spanned the theory, simulation, fabrication, and testing of novel photonic materials and devices, culminating with a dissertation on near-infrared active and tunable hyperbolic metamaterials. He derived analytical expressions for

achieving lossless wave propagation in active metal–dielectric waveguides and predicted active hyperbolic behavior with numerical simulations in the InGaAsP/Ag composite system. He then designed, fabricated, and characterized the first light-emitting hyperbolic metamaterial based on InGaAsP quantum wells, demonstrating that a deeply subwavelength lateral multilayer nanostructure can simultaneously exhibit properties of a metal and semiconductor for normally incident cross-polarized waves. In addition to light-emitting metamaterials, he contributed to the development of conformal metal-oxide metamaterials exhibiting negative refraction and broadband near-perfect absorption at telecommunication frequencies. He was also awarded a rapid access proposal to Sandia National Laboratory to explore the atomic layer deposition of silver. Prior to his work on metamaterials, he worked in the area of nanoscale semiconductor lasers and strained silicon electro-optic modulators. He contributed to the theory and design of metal-clad nanolasers, including the first analysis of the temperature dependence of the spontaneous emission factor in semiconductor laser cavities that are subwavelength in all three spatial dimensions. His work has been featured in popular science blogs, such as Phys.org, and recognized through numerous awards, including the Best Overall Paper of the SBMicro 2016 conference, finalist for Best Student Paper at SPIE Active Photonic Materials Conference 2016, and finalist for the Tingye Li Innovation Prize at CLEO 2017. Since July 2017, he has been a postdoctoral scholar at the University of California, Berkeley, working under the supervision of Prof. Xiang Zhang.

Felipe Vallini received a Ph.D. in physics (applied physics) in 2013 from State University of Campinas. Between 2013 and 2017 he was a postdoctoral researcher in the Ultrafast and Nanoscale Optics lab of Prof. Shaya Fainman at the University of California, San Diego. His areas of expertise include semiconductor physics, silicon photonics, and optical metamaterials. Currently, he is with the Intel Corporation, working as reliability engineer for optical transceivers.

Xiang Zhang is the inaugural Ernest S. Kuh Endowed Chaired Professor at UC Berkeley and the director of the NSF Nano-scale Science and Engineering Center (NSEC). He is the director of the Materials Sciences Division at Lawrence Berkeley National Laboratory (LBNL) as well as a member of the Kavli Energy Nano Science Institute. He is an elected member of the US National Academy of Engineering (NAE) and the Academia Sinica (National Academy in Republic of China) and a fellow of five scientific societies: APS (The American Physical Society), OSA (The Optical Society), AAAS (The American Association for the Advancement of Science), SPIE (The International Society of Optical Engineering), and ASME (The American Society of Mechanical Engineers). He received a Ph.D. from UC Berkeley (1996), an M.S. from the University of Minnesota, and an MS/BS from Nanjing University, China. He was an assistant professor at Pennsylvania State University (1996–1999) and an associate professor and a full professor at UCLA (1999–2004) prior to joining Berkeley faculty in 2004. His current research focuses on nano-scale science and technology, materials physics, photonics, and bio-technologies. He has published over 240 journal papers, including over 50 publications in *Science*,

the *Nature* series, *PNAS*, and *Physical Review Letters*. He has given over 280 keynote, plenary, and invited talks at international conferences and institutions. He is a recipient of the NSF CAREER Award (1997); the SME Dell K. Allen Outstanding Young Manufacturing Engineer Award (1998); and the ONR Young Investigator Award (1999). He was awarded the Chancellor Professorship by UC Berkeley (2004–2009); a Distinguished Lecturer by the University of Texas at Austin in 2004 and by SEMETECH in 2005, respectively; the Rohsenow Lecturer at MIT (2009); and the William Reynolds Lecturer at Stanford (2012). In 2011, he was awarded the Fred Kavli Distinguished Lectureship by the Materials Research Society (MRS), the Miller Professorship by UC Berkeley, and the Distinguished Visiting Scientist (DVS) by the University of Toronto. In 2014, he was awarded the Fitzroy Medal for pioneering contribution in metamaterials and superlens.

Yeshaiahu (Shaya) Fainman is an inaugural Cymer chair professor of advanced optical technologies and distinguished professor in electrical and computer engineering (ECE) at the University of California, San Diego (UCSD). He received M.Sc and Ph.D. degrees from Technion in 1979 and 1983, respectively. He is directing research of the Ultrafast and Nanoscale Optics Group at UCSD and made significant contributions to near-field optical phenomena, inhomogeneous and meta-materials, nanophotonics and plasmonics, and non-conventional imaging. His current research interests are in near-field optical science and technology with applications to information technologies and biomedical sensing. He contributed over 280 manuscripts in peer review journals and over 450 conference presentations and conference proceedings. He is a fellow of The Optical Society, a fellow of the Institute of Electrical and Electronics Engineers, a fellow of the Society of Photo-Optical Instrumentation Engineers, and a recipient of the Miriam and Aharon Gutvirt Prize, the Lady Davis Fellowship, the Brown Award, the Gabor Award, the Emmett N. Leith Medal, and the Joseph Fraunhofer Award/Robert M. Burley Prize.